

EUROPEAN ORGANIZATION FOR NUCLEAR RESEARCH

CERN LIBRARIES, GENEVA

CERN/ISRC/69-5
10 February 1969



CM-P00063293

PROPOSAL FOR AN EXPERIMENT

MEASUREMENT OF THE PRODUCTION OF
STABLE PARTICLES AT THE ISR

A.B. Clegg, C. Daum, F.C. Ern , A.D. Kanaris,
D. Locke, P.G. Murphy, J.C. Sens and F. Udo

CERN/Holland - Lancaster/Manchester Collaboration

Submitted to the ISR Committee

Geneva - February 1969

1. INTRODUCTION

In this report we investigate the feasibility of measurements on the distribution in angle and momentum of pions, kaons, protons and antiprotons produced in the ISR.

Arguments which have led to this choice over other possibilities are:

- i) The angular and momentum distribution of particles produced at 50 GeV c.m. energy is of evident importance in the light of thermodynamical, multi Regge and possibly other models of production processes at high energy.
- ii) Data of this sort will be required at an early stage in the ISR operation to enable the planning of more complicated experiments.
- iii) The data obtained will enable reliable calculations of yields for the 200 and 300 GeV machines and will supplement available data from cosmic rays by some order of magnitude.
- iv) While most experiments at the ISR will be handicapped by a low rate of events, the measurement of particle production is a relatively high rate experiment.
- v) The experiment does not require a large magnet structure affecting the ISR beams in the interaction region. Septum magnets are expected to be adequate to separate the secondary from the primary beam at small angles. Interference with the rings can thus be held to a minimum.

In the following three spectrometers will be described: a small angle spectrometer, designed to get as close as possible to zero degrees with respect to the beams in order to measure the momenta and to focus the secondaries onto Čerenkov counters for particle identification; a large angle spectrometer designed for maximum acceptance in an angular range where the rates are low; and finally an intermediate angle spectrometer, as a transition between the two. Prior to this a remark will be made about running the experiment with unequal energies in the two rings. The choice and location of

septum magnets, the Čerenkov counters, the vacuum chamber, the expected rate of events, the beam gas interactions and the monitor will also be discussed.

For definiteness we shall divide the angular range as follows:

- 0 - 15 mrad not accessible without affecting the ISR beams
- 15 - 150 mrad small angle spectrometer
- 150 - 1000 mrad medium angle spectrometer
- 1000 - 1500 mrad large angle spectrometer.

2. ISR BEAM MOMENTA

In order to obtain the maximum c.m. energy, both ISR beams must run at maximum momenta. Less than maximum c.m. energy can be obtained with a variety of beam momenta, ranging from "equal momenta" to "maximally unequal momenta" in the rings. These settings are not equivalent since for "equal momenta" the centre-of-mass is at rest, while for "maximally unequal momenta" it moves with the maximum speed compatible with the required c.m. energy. In the latter case the angle of production at the downstream side of the lower momentum ISR beam is increased by the Lorentz transformation to the lab. system, while at the downstream side of the higher momentum ISR beam the angle is correspondingly decreased. As a result a spectrometer set at a given minimum angle with respect to the ring can accept a lower value of t_{\min} (min. momentum transfer squared) in the "unequal momenta" case than in the "equal momenta" case. For example, for a spectrometer of minimum angle 30 mrad in the lab. system, one has for elastic scattering at a c.m. energy of 32 GeV:

P_1	P_2	E^*	ϑ_1	ϑ_2	ϑ^*	t
16 GeV/c	16 GeV/c	32 GeV	30 mrad	30 mrad	30 mrad	0.23 GeV/c ²
10 "	25 "	32 "	30 "	12 "	19 "	0.09 "

where ϑ_1 , ϑ_2 are the lab. angles w.r.t. the downstream side of the 10 GeV/c, respectively 25 GeV/c beams. "Unequal running" thus results in a reduction

of the minimum detectable ϑ^* from 30 to 19 mrad and a reduction in min. detectable t by a factor 2.5. Assuming an angular distribution with average slope 10 (GeV/c)^{-2} the rate of events is increased by a factor

$$\int_{0.09}^{\infty} e^{-10t} dt \Big/ \int_{0.23}^{\infty} e^{-10t} dt \approx 3.5 \quad (1)$$

Figure 1 indicates the minimum detectable t at various c.m. energies, for equal and maximally unequal momenta in the rings, assuming a minimum spectrometer angle of 30 mrad. For inelastic events the distribution in t is less steep and hence the gain is less.

3. SMALL ANGLE SPECTROMETER

It is well known that in the very forward direction the rate of events is expected to be high over the entire spectrum of momenta, due to the combined contributions of leading protons and secondaries emitted in high multiplicity events and of nucleons and decay products from isobar production. With an average transverse momentum $p_T \approx 0.3 \text{ GeV/c}$, this region extends over an angular interval $\leq 20 \text{ mrad}$; hence the importance of reaching the smallest possible angles with the spectrometer.

It is proposed here to deflect the secondaries into the vertical direction by means of septum magnets placed above one of the rings. The septum magnets are followed by bending magnets and quadrupoles for momentum analysis and by Čerenkov counters, onto which the secondaries are focused for particle identification.

The advantages of vertical over horizontal deflection are the following:

- i) For vertical bending the size of the source in the direction of bending is smallest; this simplifies the optics.
- ii) Clearance of the next downstream ISR element at 9.8 m from the intersection. A standard ISR magnet is 0.61 m high and 0.53 m wide at the open

side (measured from the centre of the vacuum chamber). Without septum magnets the minimum detectable angle would then be 50-60 mrad and hence a major part of the angular distribution would remain inaccessible. It will be shown in Section 8 that with two septum magnets the minimum detectable angle can be reduced to ~ 15 mrad provided the bending is done in the vertical plane. For the horizontal plane the minimum angle would be ~ 25 -30 mrad. "Skew" bending offers no particular advantages.

iii) Signal/background. As will be shown in Section 9 the ratio of beam-gas to beam-beam interactions seen by the spectrometer placed above the rings is reduced by a factor of roughly two compared to the ratio seen in the horizontal plane.

An alternative to using septum magnets is the use of a "special magnet"¹⁾ i.e. a large magnet which replaces the first two downstream ISR elements. The field is fixed in sign and magnitude. Particle trajectories for various angles and momenta show that a large fraction of the particles will leave the magnet sideways and can only be collected into a Čerenkov counter by a rotatable set of magnets; this solution has been rejected as impractical.

The small angle spectrometer is shown in Fig. 2. It consists of 2 septum magnets (to be described below), two 1.5 m long/20 cm diameter and two 2 m long/20 cm diameter standard quadrupoles, and three 2 m long standard bending magnets. The septum magnets and the first two quadrupoles are mounted on supports which allow for displacement in the vertical and horizontal direction and rotation around a horizontal axis perpendicular to the beam. The two septum magnets and the first quadrupole are placed in the space between the intersection and the next downstream ISR element at 9.8 m; the remaining elements are placed on top of the downstream ISR elements.

The optical characteristics are shown in Figs. 3, 4 and 5 and in Table 1. Figure 3 shows the deflections in the septum and bending magnets corresponding to a particle produced at 20 mrad. Figure 4 shows trajectories in both planes, of particles emitted at 4 mrad with respect to the production angle for which

the septum and bending magnets are set. Figure 5 shows trajectories from the front and rear end of the intersecting volume, 60 cm apart. With the currents in the magnets set near the design values given in Table 2, the focus for 25 GeV/c particles is at 41.5 m from the centre of the intersection. For particles produced at the front and rear ends of the intersecting region the focal planes are displaced by ± 1.7 m; at these positions the apparent object size is +10%, respectively, -10% different in size from the image of the centre of the intersecting region.

The counters and spark chambers shown in Fig. 2 determine the scattering angle and the momentum. The resolving power of the spectrometer is illustrated in Fig. 6B which shows the phase space diagram for the vertical plane (plane of bending) at the focus, for particles with 23, 24, 25, 26 and 27 GeV/c momentum, with the spectrometer set at 25 GeV/c. Figure 7B shows the same for the horizontal plane for 23, 25 and 27 GeV/c. Inspection of these figures shows that a set of five 7 cm (H) \times 8 cm (V) scintillators placed one above the other would already give a resolution of $\sim 4\%$ in momentum, a figure which can easily be reduced to $\sim 1\%$ without necessitating the use of chambers. This is of use in on-line classification of the data. Two pairs of spark chambers placed before and after the bending magnets will improve this further. If the distance between the two chambers in each pair is l and α_1, α_2 are the entrance, respectively, exit angles of the (combined) bending magnets, then if $\alpha = \alpha_1 - \alpha_2$

$$\frac{dp}{p} = \frac{d\alpha}{\alpha} = \sqrt{2} \frac{dl}{l} \quad (2)$$

hence with a spark chamber resolution of $dl = \pm 1$ mm and $l = 1$ m

$$\frac{dp}{p} = \pm 0.14 \% \quad (3)$$

which is certainly adequate.

The scattering angle θ is measured by the coordinates of the sparks in the first two chambers in Fig. 2. Its accuracy is given by

$$\left(\frac{d\theta}{\theta}\right)^2 = \left(\frac{dl}{l}\right)^2 + \left(\frac{d\theta_c}{\theta}\right)^2 \quad (4)$$

where $d\theta_c$ is the mean angle of multiple scattering in the walls of the vacuum chamber (see Section 7) and where it has been assumed that no error is introduced by the integral $\int Bdl$ for the septum magnets. For the vacuum chamber (3 mm stainless steel traversed perpendicularly, see below) we have

$$d\theta_c \approx \frac{20}{p} \sqrt{0.15} \approx \frac{3}{p}, \quad p \text{ in GeV/c, } d\theta_c \text{ in mrad} \quad (5)$$

Hence

$$\left(\frac{d\theta}{\theta}\right)^2 = \left(\frac{dl}{l}\right)^2 + \left(\frac{\delta}{p\theta}\right)^2 \quad (6)$$

For $dl/l \approx 10^{-3}$ this error is dominated by the multiple scattering, except at angles near 150 mrad and momenta near 25 GeV/c. In fact, for most angles and momenta a ~ 10 mm precision in the coordinates would be adequate. We have for the error:

$$\begin{aligned} d\theta &= 0.3 \text{ mrad} & \text{for } p &= 25 \text{ GeV/c} \\ &= 1.5 \text{ mrad} & \text{for } p &= 5 \text{ GeV/c} . \end{aligned} \quad (7)$$

An important point in connection with the conversion of the observed rates to differential cross-sections is the variation of solid angle $\Delta\Omega$ and accepted momentum bite Δp with the position of the point of interaction in the intersection volume. For the total collision rate we have:

$$N = 2\pi c \cos^2 \frac{\alpha}{2} \int n_1(x, y, z) n_2(x, y, z) dx dy dz \quad \text{collisions/sec} \quad (8)$$

where

σ = total cross-section

c = velocity of the proton

α = angle of intersection = 15°

$n_{1,2}(x,y,z)$ = No. of protons per unit volume in ring 1, 2

and where the integral extends over the intersecting region (IR).

If the total number of protons in either ring, N_s , is uniformly distributed over the circumference $2\pi R$, the beam height h and the beam width w we have

$$N_{\text{UNIFORM}} = 2\pi c \cos^2 \frac{\alpha}{2} \left(\frac{N_s}{hw 2\pi R} \right)^2 \frac{hw^2}{\sin \alpha}$$

$$= \frac{J_e}{h \tan \frac{\alpha}{2}} \left(\frac{N_s}{2\pi R} \right)^2 = L \bar{\sigma}$$
(9)

which is the familiar expression for the luminosity²⁾. Equation (9) has been used in estimating the rates (see Section 9) assuming $\Delta\Omega$ and Δp to be independent of the position of the interaction point. Although good enough for this estimate, Eq. (9) is only an approximation as can be seen from Figs. 6A and 7A which show the fraction of the vertical, respectively, horizontal phase space at the interaction, as seen by the spectrometer; in particular in the horizontal plane there is a strong correlation between position on the one hand and angular acceptance and momentum on the other. Taking this into account we have for the rate of events

$$R(p,\theta) = 2c \cos^2 \frac{\alpha}{2} \frac{d^2\sigma(p,\theta)}{dpdQ} \int_{IR} n_1(x,y,z) n_2(x,y,z) \Delta p(x,y,z) \Delta Q(x,y,z) dx dy dz$$
(10)

where

$[d^2\sigma(p, \vartheta)/dpd\Omega]$ = differential cross-section for production of secondaries (of a particular type) produced at angle ϑ and with momentum p .

The limits of integration are given by:

$-h/2 < z < +h/2$ where $h \approx 14$ mm, the height of the beams.

$-h/2 < x < l/2$ where $l \approx 600$ mm, the length (along the circumference) of the intersecting volume.

$-w(x)/2 < y < w(x)/2$ where $w(x)$ is the width of the intersecting volume at position x .

The functions $\Delta p(x, y, z)$ and $d\Omega(x, y, z)$ can be calculated for given settings of the spectrometers magnets by similar methods as used for obtaining the diagrams in Figs. 6A and 7A. The product of the beam profiles, $n_1(x, y, z) n_2(x, y, z)$ must be measured (see Section 10) and folded into Eq. (10). From the observed rate and Eq. (10) one then obtains $[d^2\sigma(p, \vartheta)/dpd\Omega]$; in case of unequal beam momenta this quantity must then be further Lorentz transformed to the c.m. system. It may be noted that no knowledge of the coordinates of the point of interaction is required, once the functions n_1 , n_2 , Δp and $\Delta\Omega$ are known by measurements and calculations.

To a limited extent the spectrometer is self-monitoring. By classifying particles of a given kind produced with the same momentum and angle, but having originated along different slices which can be drawn through the intersecting volume parallel to the axis of the spectrometer, one obtains rates whose ratio's are independent of the production cross-section (which is a function of p and ϑ only). For example, for two such slices

$$\frac{R_1(p, \vartheta)}{R_2(p, \vartheta)} = \frac{\int_1 n_1(x, y, z) n_2(x, y, z) \Delta p(x, y, z) \Delta \Omega(x, y, z) dx dy dz}{\int_2 n_1(x, y, z) n_2(x, y, z) \Delta p(x, y, z) \Delta \Omega(x, y, z) dx dy dz} \quad (11)$$

where the limits of integration now extend over the volume of the two slices. One thus measures integrals over slices through the beam profiles, not the profiles themselves. This feature does therefore not replace the need for a profile measurement, but it provides a built-in check on the stability of the shape of the beams with time. The accuracy with which the "slice" through the interacting volume can be located depends mostly on the precision in the coordinates in the first two spark chambers. With ± 1 mm precision in this pair (1 m apart) one has a 15 mm uncertainty in the intersection 15 m away. It will thus be useful, if background problems do not prevent this, to place spark chambers in front of the two septa as well.

The Čerenkov counters will be discussed below. Helium bags or vacuum will be required since the air path over 40 m is 0.13 radiation lengths, equivalent to an extra 2.5 mm stainless steel.

4. LARGE ANGLE SPECTROMETER

At large angles (1000-1500 mrad) the distributions of secondaries are characterized by:

- 1) A very steep decrease in intensity of all but the lowest momentum particles with increasing angle.
- 2) A relatively weak dependence of intensity on angle and momentum within the range of low momenta, indicating the predominance of high multiplicity type of events in this region of the spectrum. A practical upper limit on the momentum for measurable fluxes at large angles is ~ 3 GeV/c.

Figure 8 indicates one possible design which meets the requirements of large solid angle and wide momentum acceptance, indicated by the above-mentioned features of the production process. Its main objective is to provide momentum analysis, while at the same time holding the trajectories together over a long enough path so that the particle can be identified by time of flight. It consists of two 1 m long quadrupoles with non-standard aperture (0.35 m \emptyset), followed by a 1 m long standard bending magnet of 0.5 (H) \times 0.2 (V) m aperture. The spectrometer accepts particles from the

central region (~ 20 cm) of the area of the intersecting beams. The solid angle as a function of momentum is shown in Fig. 9. It is seen that a range of ~ 0.7 GeV/c is accepted with more than $\sim 50\%$ of the full solid angle. Momenta up to ~ 3 GeV/c can thus be collected with three to four settings of the spectrometer.

It must be stressed that the set-up of Fig. 8 is by no means the only possible one. In particular, one could omit the quadrupoles and move the bending magnet forward up to ~ 2 m from the intersection. This would, however, not increase the solid angle and only shorten the path available for identification by time of flight. A more elaborate hodoscope of time of flight counters would then be required after the bending magnet to identify the particles over the whole range of momenta. If a larger, non-standard, bending magnet would be available, such a solution might, in fact, be preferred. The rates calculated for the set-up of Fig. 8 (see Section 9) indicate, however, that the present arrangement is probably adequate. It may be noted that the solid angle is $\sim 100 \times$ as large as the one for the small angle spectrometer.

Figure 8 shows the position of the counters and the spark chambers. The interaction point is determined by WC1 and WC2 with a precision of the order of a few millimeters in the x (along the machine circumference) and z (vertical) directions. This is to be compared with the precision of 15 mm quoted above for the small angle spectrometer. As will be discussed further, below (see Section 10) this is a strong argument (besides obvious economy considerations) for running both spectrometers at the same time, so that the large angle spectrometer can act as monitor while data are being collected at small and large angles simultaneously.

The momentum is determined by WC3-WC6 in Fig. 8. The accuracy obtained is given by Eq. (2), with $l = 2$ m:

$$\frac{dp}{p} = \pm 0.07 \% \quad (12)$$

The scattering angle is determined by WC1 and WC2, with an accuracy [c.f. Eq. (4)]:

$$\left(\frac{d\theta}{\theta}\right)^2 = \left(\frac{dl}{l}\right)^2 + \left(\frac{\delta}{p\beta c}\right)^2 \approx \left(\frac{\delta}{p\beta c}\right)^2 \quad (13)$$

For example:

$$\begin{aligned} d\theta &= 2.7 \text{ mrad} && \text{for } 3.0 \text{ GeV/c } \pi \\ &= 120 \text{ mrad} && \text{for } 0.25 \text{ GeV/c } p . \end{aligned} \quad (14)$$

For momenta down to ~ 0.25 GeV/c the vacuum chamber thus introduces an error of less than $\sim 10\%$.

Between ~ 2 and 3 GeV/c particles are identified by means of two gas Čerenkov counters (see Section 6). Between 1 and 2 GeV/c pions are labeled by one Čerenkov counter, kaons and protons are distinguished by time of flight. The time difference ranges from ~ 2.5 to ~ 8 nsec over a ~ 9 m flight path. Below ~ 1 GeV/c pions, kaons and protons have flight times which differ by at least 3.5 nsec and are hence easily measurable.

At 1.8 GeV/c 50% of the kaons have decayed before reaching the second time-of-flight counter; at 0.5 GeV/c this is 92% . By placing a third time-of-flight counter at, e.g. 2 m this loss is reduced to 42% , while the π -K flight time difference remains ≥ 2.5 nsec for momenta ≤ 0.5 GeV/c.

The optical and electrical characteristics of the large angle spectrometer are summarized in Table 3. Figure 10A shows the fraction of phase space in the horizontal plane at the intersection, accepted with the spectrometer set at 1 GeV/c for particles of various momenta. Figure 10B shows the phase space at 1.25 m behind the bending magnet. Note the reduction in dispersion with respect to the small angle spectrometer (Fig. 6B), due to the smaller bending power and the larger acceptance.

5. MEDIUM ANGLE SPECTROMETER

In the range 150-1000 mrad the thermodynamical model predicts again a very steep decrease in intensity with increasing angle for all high and intermediate momentum particles. At ~ 150 mrad the highest measurable momentum is ~ 15 GeV/c; at ~ 1000 mrad it is ~ 3 GeV/c. In this angular range the interpretation of the data is complicated by the fact that both isobar-formation and high multiplicity reactions contribute to the production of particles. It is proposed to scan the medium angle range in fairly large steps.

The layout is sketched in Fig. 11 and the optical and electrical characteristics are indicated in Table 4. It consists entirely of standard elements, four 1.5 m long, 0.2 m aperture quadrupoles and one 2 m long, 0.33 (H) \times 0.14 (V) m aperture bending magnet. Particles are accepted over the full height and width of the intersecting beams. The ray diagram is shown in Fig. 12; it is seen that the main limitation in rate comes from the apertures of Q_3 and Q_4 . The phase space at the intersection in the horizontal (bending) plane accepted by the spectrometer when set at 10 GeV/c, is shown in Fig. 13A for 9, 10 and 11 GeV/c particles; Fig. 13B shows the horizontal phase space at the focus, 25 m from the intersection. As in the large angle set-up the increased acceptance worsens the optics at the foci compared to the small angle spectrometer. Nevertheless a simple counter set-up, e.g. one 14 (H) \times 1 (V) cm scintillator on the central ray at the focus, and one of 20 (H) \times 4 (V) cm on each side, is sufficient to obtain a $\sim 10\%$ resolution in momentum. The scattering angle is again determined by spark chambers to a precision of $\lesssim 3$ mrad limited only by the vacuum chamber.

6. ČERENKOV COUNTERS

In all three spectrometers particles are identified by means of Čerenkov counters. In order to judge whether threshold counters are adequate and, if so, what length and what gas pressure they should have, threshold curves have

been calculated for various gases and various lengths of the counter. In these calculations it has been assumed that the quantum efficiency (No. of photoelectrons per photon) for a typical photomultiplier is 18%, that the optical efficiency is 50% and that 10 photoelectrons are required for a "yes" signal and 0 photoelectrons for a "no" signal. One then obtains from standard formulae for the critical angle and the number of photoelectrons, collected in a counter of length l cm:

$$\theta_c = \sqrt{2(\epsilon - \delta)} \quad (15)$$
$$N_e = 75l(\epsilon - \delta) \text{ photoelectrons}$$

with

$$\epsilon = n-1 \quad ; \quad \delta = 1-\beta \quad (16)$$

and

$$\epsilon = K P \quad P = \text{pressure (kg/cm}^2\text{)}$$

where K is a constant, characteristic for the gas in question.

We have

$$\begin{aligned} K &= 1.47 \times 10^{-4} \text{ for H}_2 \\ &= 7.0 \times 10^{-4} \text{ for aethylene} \\ &= 10.0 \times 10^{-4} \text{ for propane} \\ &= 13.3 \times 10^{-4} \text{ for isobutane .} \end{aligned}$$

The condition for a "yes" signal is then: $N_e = 10$, i.e.

$$P = \frac{\delta}{K} + \frac{10}{75Kl} \quad (\text{kg/cm}^2) \quad (18)$$

and for a "no" signal ("no light" limit): $N_e = 0$, i.e.

$$P = \frac{\delta}{K} \quad (\text{kg/cm}^2) \quad (19)$$

Figure 14 shows the results for the four gases listed above. It is seen that there is a wide choice of configurations which will distinguish π , K and p over the typically $\pm 10\%$ momentum acceptances of the small and medium angle spectrometers, down to ~ 2 GeV/c. In the choice of gas, hydrogen is to be preferred in view of its high refractive power per atomic electron. This is of importance for the detection of rare particles in the presence of a high rate of other particles below threshold. It is furthermore seen from Fig. 14 that the simultaneous requirement of 10 photoelectrons for a "yes" and 0 photoelectrons for a "no" signal restricts the choice of lengths of counters to be used above ~ 20 GeV/c. In particular, the π counter must be at least 7.5 m long and the $\pi + K$ counter at least 2.5 m long in the small angle spectrometer, where particles up to 25 GeV/c are to be identified. This is independent of the choice of gas. Below 13-15 GeV/c (medium angle spectrometer) both the π and the $\pi + K$ counter need not be longer than 2.5 m.

The diameter of the counters is determined by the phase space diagrams at the focus (Figs. 6A and 13B). A 7.5 m long counter placed beyond the focus of the small angle spectrometer requires a 10 (H) \times 50 (V) cm aperture; the divergence at this point is < 15 mrad. For reasons of mechanical strength and optical efficiency a conically shaped counter with front window ϕ 30 cm and rear window ϕ 50 cm is possibly most suitable for this purpose. It is known from tests that a 5.0 mm Al window is required to maintain a ~ 30 atm pressure if its diameter is 50 cm.

Below 2 GeV/c time-of-flight identifies the particle in the 40 m long small angle and 25 m long medium angle spectrometer. In the 9 m long large angle spectrometer particles below 2 GeV/c are identified by a combination of one Čerenkov counter and time-of-flight, as mentioned in Section 4.

Since the low rates at the ISR exclude any testing on site, it is intended to test the Čerenkov counters (along with all other counters and chambers) at the SC or the PS. In particular the question whether the production of

δ -rays makes it necessary to install low field sweeping magnets between Čerenkov counters can then be settled empirically.

7. VACUUM CHAMBER

The standard ISR vacuum pipe consists of 3 mm thick stainless steel. This corresponds to 0.15 radiation length and ~ 0.03 collision length. A particle emitted at 20 mrad, traverses 15 cm wall, corresponding to a 70% probability of interaction and a multiple scattering angle of 2.2 mrad for a 25 GeV/c, 5.5 mrad for a 10 GeV/c particle. In the interaction region the standard ISR pipe must therefore be replaced by a special vacuum chamber.

What maximum wall thickness is acceptable? From the derivative of the betatron amplitude, taken at the intersection, it can be shown³⁾ that the maximum uncertainty in angle at the production point for the ISR design parameters, for the horizontal (x) and vertical (z) planes, is given by:

$$\begin{aligned} X' &= 0.49 \text{ mrad at } 10 \text{ GeV} ; & Z' &= 0.49 \text{ mrad at } 10 \text{ GeV} \\ &= 0.38 \text{ mrad at } 25 \text{ GeV} & &= 0.35 \text{ mrad at } 25 \text{ GeV} \end{aligned} \quad (20)$$

The walls should thus introduce no more multiple scattering than these inherent angular uncertainties. A 3 mm stainless steel wall, traversed perpendicularly produces a multiple scattering of 0.3 mrad for 25 GeV/c protons and 3.5 mrad for 2.5 GeV/c protons and thus contributes an error of less than 10% to the scattering angle for momenta > 2.5 GeV/c and angles > 35 mrad. For angles ≤ 35 mrad in the small angle spectrometer the wall should simply be as thin as is mechanically tolerable.

A vacuum chamber suitable for use with any one of the three spectrometers is indicated in Fig. 15. It consists of an octagonally shaped box, to which the upstream ISR pipes are attached. The downstream ISR pipes are replaced

by "flares" which enable the particles emitted in the vertical plane to traverse the vacuum walls perpendicularly before entering the measuring devices above and eventually below the downstream beams; they also contain a section which can be displaced vertically (but left in place during injection) by means of bellows, in order to accommodate the septum magnets on one side and spark chambers or counters on the other side as close as possible to the downstream beams. Between this section and the end of the flare the standard pipe is maintained. The flare is placed at least at 1.70 m from the intersection since no particle can traverse the pipe beyond this distance and still enter the septum magnet, anywhere over its 6 cm width.

The chamber is kept as small as possible in order not to obstruct any detectors. Its minimum half length L in the direction of the beams ($L = 0.6$ m) is specified by the point where the up- and downstream pipes touch. In the region of large angles, its size has been reduced below L in order to gain space for the large angle spectrometer. In doing so the effective wall thickness is increased by no more than 10%, i.e. a $< 5\%$ increase in multiple scattering. The height of the chamber (± 150 mm) and of the end of the flare (± 300 mm) are set by the requirement that particles from the entire interaction volume, emitted between $15 < \vartheta < 150$ mrad and $50^\circ < \varphi < 130^\circ$ (corresponding to a 6 cm width septum with front face at 2.25 m; $\varphi = 90^\circ$ is the vertical direction) must be able to enter the small angle spectrometer.

As discussed below, it is of great importance to maintain a vacuum of $\leq 10^{-11}$ Torr N_2 in the interaction region; hence cryopumps will be connected to the chamber as close as possible to the interaction volume. Pressure tests should be performed at an early date with helium and/or nitrogen-titanium pumps.

8. SEPTUM MAGNETS

In this paragraph we return to the problem of the septum magnets in the small angle spectrometer. In particular the optimum dimensions of the septa, their optimum position with respect to the intersection, and the required power are calculated and compared for bending in the horizontal and vertical plane. It is assumed that at most two septum magnets will be used for sweeping charged secondaries produced at small angles past the first obstacle, the ISR magnet, in the downstream side of an ingoing intersection.

Figure 16 shows the general layout of the system and the notation used. It is seen that the following conditions must be satisfied:

$$\alpha_0 L_0 + \alpha_1 L_1 + \alpha_2 L_2 \gg H \quad (21)$$

$$\alpha_0 = (H_1 + d_1) / (L_0 - L_1 - 0.5 l_1) \quad (22)$$

$$L_2 + 0.5 l_2 = L_1 - 0.5 l_1 - 0.5 \quad (23)$$

if a distance of 0.5 m is required between the septum magnets. Furthermore

$$l_{2 \max} = L_1 - 0.5 l_1 - 1 \quad (24)$$

if also a minimum distance of 0.5 m between the second septum and the first ISR magnet is required. Finally:

$$H_2 + d_2 = \alpha_0 (L_0 - L_1 + 0.5 l_1 + 0.5) + \alpha_1 (0.5 l_1 + 0.5) \quad (25)$$

The smallest distance, H_1 , between the septum and the centre of the beam is illustrated in Fig. 17 for vertical and horizontal bending. The calculations have been done for a beam size of 74 mm horizontal and 14 mm vertical, corresponding to a stacked beam with $\Delta p/p = 2\%$ including betatron oscillation

amplitude, injection errors and blow-up of the beam due to Coulomb scattering with the rest gas in the vacuum pipe. It has been assumed that the wall of the vacuum system can be moved down to 2.5 mm distance from the edge of the beam. The wall thickness is taken to be 3 mm and the minimum distance between the septum and the vacuum pipe is 2.5 mm. (Alternatively, the beam can be steered towards the wall of the vacuum pipe, hence effectively decreasing the size H of the obstacle.) Figure 17 shows that $H_v = 15$ mm for vertical bending and $H_h = 45$ mm for horizontal bending, and values in between for bending in a plane between horizontal and vertical ("skew" bending).

A comparison between horizontal, vertical and skew bending is made in Fig. 18. The figure shows the front end of the first downstream ISR magnet. The small circle shows the displacement $\alpha_0 L_0$ of the secondaries away from the central orbit due to the production angle. The four ellipsoids show the displacement $\alpha_0 L_0 + \alpha_1 L_1$ due to four possible septa listed in Table 5. For a good comparison, it is important to take into account not only the size of the obstacle [H in Eq. (21)] but also the size of the first quadrupole doublet in the spectrometer. In the figure their positions, Q_V , Q_S and Q_H , are indicated for the axis of a standard split pole quadrupole magnet at the earliest longitudinal position along the ISR where they can fit. For horizontal bending the largest displacement is obtained for septum C ($\alpha_1 = 107$ mrad). The direction at the entrance of the ISR magnet is now 122 mrad, the entrance of Q_H can then be put at 2.75 m beyond the entrance of the ISR magnet. Similarly for Q_S with septum A, B, C, D the distances are 2.72 m, 1.45 m, 0.86 m, 0.70 m, respectively, and for Q_V with septum D the distance is 1.57 m.

At first view, "skew" bending is to be preferred over vertical bending because of power economy, but for simplicity of optics vertical bending is to be preferred. With thinner septa, the power can be reduced. We have used a paper by Green⁴⁾ to estimate maximum conditions for a first septum, i.e. with d_1 and l_1 matched to the maximum field of 1.8 T. The result is

shown in Table 6. The lowest power is obtained for cases a and b. The power is higher than for "skew" bending but in the case of vertical bending a first Q magnet can be introduced before the ISR magnet. It is not excluded that for "skew" bending, a similar study would give improvement. However, in that case H_1 [Eq. (22), Fig. 17] is larger than for vertical bending and less space is available for two septum magnets and a quadrupole magnet.

The septum magnets have been readjusted finally to slightly less rigorous conditions, keeping in mind that a 20 A, 600 kW generator will be available. Table 7 shows the result. The power dissipated in the septum has been increased by 20% as an estimate of the additional loss in return windings and in- and output leads. This system is also optimized for the production angle. It is in practice not possible to go much lower than $\alpha_0 = 15$ mrad. The positions of the two septa, resulting from the optimization procedure are:

$L_1 = 6.8$ m i.e. centre of first septum is at 3.0 m from intersection.

$L_2 = 4.0$ m i.e. centre of second septum is at 5.8 m from intersection.

The mechanical strength of a multiturn septum is not sufficient to stand the magnetic pressure. This pressure is

$$p_B = \frac{1}{2} BH = \frac{1}{2} \frac{B^2}{\mu} \frac{N}{h^2} \approx 13 \text{ kg/cm}^2 \text{ for } B = 1.8 \text{ T} \quad (26)$$

The septum can be supported on the outside by a stainless steel plate. The displacement, f , at the centre of the plate under pressure is given by:

$$f = p_B \frac{k^4}{32 E d_s^3} \quad (27)$$

where h is the height of the septum, d_s is the thickness of the stainless steel plate and E is Young's modulus ($\approx 2 \times 10^6$ kg/cm² for steel).

For $f \leq 0.2$ mm, the plate thickness, d_s , has been indicated in Table 7. This supporting plate fits between the septum and the ISR vacuum pipe. The septa can be positioned to follow the direction of the secondary particles.

Hence, the supporting plates can be made wedge shaped with increasing d_s from beginning to end. The stress on the stainless steel plate, also indicated in Table 7 is

$$S = \left(\frac{3}{4}\right) p_B \left(\frac{h}{d_s}\right)^4 \quad (28)$$

The stress is in all cases far below the maximum permissible stress for the usual steels ($S_{\max} \approx 10^5 \text{ kg/cm}^2$).

9. RATE OF EVENTS, BACKGROUND

The design value of the luminosity L of the ISR for beam-beam interactions is [see Eq. (9)]:

$$L_{bb} = 4 \times 10^{36} / \text{cm}^2 \cdot \text{sec}$$

for 4×10^{14} protons in each circulating beam. The total cross-section at 50 GeV c.m. energy is unknown. Cosmic-ray data indicate $\sim 30 \text{ mb}$, an extrapolation of accelerator data gives 38 mb , a theory by Cabibbo et al. suggests $\sim 25 \text{ mb}$ ⁵⁾. We take 30 mb . The rate of secondaries produced per day is then

$$R(p, \vartheta) = 2.1 \times 10^{10} \times f \times p \times \Delta\Omega \times N(p, \vartheta) \quad \text{secondaries/day} \quad (29)$$

where

p = momentum of the secondary particle (GeV/c)

f = momentum interval, in units of p ($\Delta p/p = \pm f$)

$\Delta\Omega$ = solid angle (sr)

$N(p, \vartheta)$ = number of secondaries produced/sr.GeV/c.int.proton.

$N(p, \vartheta)$ is taken from the thermodynamical model of Hagedorn and Ranft⁶⁾, as calculated in a programme written by J. Ranft⁷⁾ and adapted to ISR geometry by S. Andersson and C. Daum⁸⁾. With the values for f and $\Delta\Omega$ indicated in

Tables 1, 3 and 4 we have

$$R(p, \theta) = C p N(p, \theta) \quad \text{events/day} \quad (30)$$

with

$$\begin{aligned} C &= 6.25 \times 10^4 && \text{for the small angle spectrometer} \\ &= 2.62 \times 10^5 && \text{for the medium angle spectrometer} \end{aligned} \quad (31)$$

while for the large angle spectrometer C itself is dependent on p . As a representative figure we take $f = 0.15$, $\Delta\Omega = 6.6$ msr (see Fig. 9) and hence

$$C = 2.0 \times 10^7 \quad \text{for the large angle spectrometer} \quad (32)$$

This choice will probably not overestimate the rate at large angles (within the limitations of the model).

The rates obtained are indicated in Tables 8, 9 and 10. The very strong dependence of rate on angle and momentum is evident. If a rate of 100 events per day can be considered to be a practical lower limit, then p , π^+ , K^+ and \bar{p} emitted with momenta between 2.5 and 10 GeV/c are measurable over the entire angular range of the small angle spectrometer. For the medium angles the rates are negligibly small down to ~ 10 GeV/c at 150 mrad and down to ~ 1 GeV/c at 1000 mrad. At large angles the rate is negligible down to ~ 3 GeV/c; below this momentum the rate is only weakly dependent on angle.

At a gas pressure in the intersecting regions of 10^{-11} Torr N_2 , the effective luminosity for beam-gas interaction is

$$L_{bg} = 10^{26} / \text{cm}^2 \text{ sec. cm beam} \quad (33)$$

The geometrical cross-section for proton-N₂ collisions is 380 mb and thus the background in each spectrometer is expected to be:

$$35/\text{sec.cm beam seen by the spectrometer .} \quad (34)$$

The secondaries produced by these 35 p-N₂ interactions give rise to a background equal to

$$R_B(p, \vartheta) = 6.08 \times 10^6 \times f \times p \times \Delta\Omega \times N_B(p, \vartheta) \times l / \text{day} \quad (35)$$

where f , p $\Delta\Omega$ are the same as above

$N_B(p, \vartheta)$ = number of secondaries produced in p-N₂/sr.GeV/c.int.proton

l = length of beam(s) seen by the spectrometer.

For the values of f and $\Delta\Omega$ listed in Tables 1, 3 and 4 we have:

$$R_B(p, \vartheta) = C_B p N_B(p, \vartheta) l \quad (36)$$

with

$$\begin{aligned} C_B &= 18 && \text{for the small angle spectrometer} \\ C_B &= 76 && \text{for the medium angle spectrometer} \\ C_B &= 6 \times 10^3 && \text{for the large angle spectrometer .} \end{aligned} \quad (37)$$

Here, l can be calculated for each scattering angle from the geometry of the intersecting region. For bending in the horizontal (l_H) and vertical (l_V) direction one has

$$l_H = w \left(\frac{1}{\text{tg} \alpha} + \frac{1}{\text{sin} \alpha} \right) + \frac{w}{\text{tg} \vartheta} \quad (38)$$

$$l_V = w \left(\frac{1}{\text{tg} \alpha} + \frac{1}{\text{sin} \alpha} \right) + \frac{h}{\text{tg} \vartheta} \quad (39)$$

and hence

$$l_H - l_V = \frac{w - h}{\tan \vartheta} \quad (40)$$

where

w = width of either beam (taken to be equal) = 75 mm

h = height of either beam (taken to be equal) = 14 mm

α = crossing angle = 15°

ϑ = scattering angle.

Equation (40) displays the advantage of vertical over horizontal bending (see Section 3), from the view point of signal/background; e.g. for 15 mrad

$$l_H - l_V = 4 \text{ m} \quad (41)$$

while from Eq. (39)

$$l_V = 1.5 \text{ m} \quad (42)$$

The results, computed with Eqs. (30), (31), (36), (37), (38) (for the medium and large angle spectrometer) and (39) (for the small angle spectrometer) with values for $N(p, \vartheta)$ and $N_B(p, \vartheta)$ obtained from the programme of Ref. 8 are listed in Tables 8, 9 and 10.

From these results it can be concluded that, in the hypothesis that the thermodynamical model gives a correct estimate of the rates, the beam-gas interactions are less than 5% of the beam-beam interactions for all particles at all momenta and all scattering angles with the exception of protons below 2.5 GeV/c where this ratio increases to 110-120% (for 0.25 GeV/c at 25 mrad). Hence if a vacuum of 10^{-11} Torr N_2 can indeed be reached in the intersection, no elaborate background measurements would then be necessary. The criteria,

imposed by the spectrometers on accepting good events, evidently aid quite strongly in rejecting background.

10. MONITOR

The quantity measured in the experiment is given by Eq. (10):

$$R(p, \theta) = 2c \cos^2 \frac{\alpha}{2} \frac{d^2 \sigma(p, \theta)}{dp d\Omega} \int_{IR} n_1(x, y, z) n_2(x, y, z) \Delta p(x, y, z) \Delta \Omega(x, y, z) dx dy dz \quad (43)$$

↓

measured in
spectrometers

↓

to be
determined

↓

to be measured
with monitors

↓ ↓

known from properties
of spectrometer

The symbols have been defined after Eq. (10). It is evident from Eq. (43), that a measurement of the overlap integral [see Eq. (45) below], for which methods have been devised by several authors^{9,10}) is not sufficient to evaluate the differential cross-sections from the observed rates; this is since not only the densities but also the acceptance in momentum, Δp , and solid angle $\Delta \Omega$, of the spectrometers are functions of the coordinates of the point of interaction. In this case it is in fact the differential overlap function $n_1(x, y, z) n_2(x, y, z)$ which is required in Eq. (43). This function is determined by setting up a monitor which measures a rate proportional to the number of secondaries emerging from each volume element of the interaction region. The proportionality constant is then obtained from the integrated rate and a measurement of h_{eff} . The complete measurement is thus done in the following three steps.

- 1) A monitor telescope is constructed whose solid angle is independent of the coordinates x, y, z of the point of interaction and in which the charged particle rate integrated over all momenta and over the whole interaction volume is measured. We then have for the rate in this monitor:

$$R_M(\theta) = 2c \cos^2 \frac{\alpha}{2} \frac{d\sigma_c}{d\Omega} \Delta \Omega_M \int n_1(x, y, z) n_2(x, y, z) dx dy dz \quad (44)$$

where $d\sigma_c/d\Omega$ is the differential cross-section for the production of charged particles (of any kind) and $\Delta\Omega_M$ the solid angle subtended by the monitor.

2) We determine the overlap integral

$$\int n_1(x, y, z) n_2(x, y, z) dx dy dz \quad (45)$$

in Eq. (44) through a measurement of h_{eff} by the methods proposed in Ref. 9 or 10.

The relation between Eq. (45) and h_{eff} is found by equating Eq. (8) to Eq. (9) which defines h_{eff} :

$$h_{\text{eff}} \frac{c\sigma}{I_9 \frac{\alpha}{2}} \left(\frac{N_{S_1}}{2\pi R} \right) \left(\frac{N_{S_2}}{2\pi R} \right) = 2\sigma c \cos^2 \frac{\alpha}{2} \int_{IR} n_1(x, y, z) n_2(x, y, z) dx dy dz \quad (46)$$

where [unlike in Eq. (9)] we have taken the total No. of protons in the two rings, N_{S_1} and N_{S_2} , to be different.

Equations (43) to (46) are independent of the choice of reference frame. We now fix a frame (x_1, y_1, z_1) to ring 1 and introduce a second frame (x_2, y_2, z_2) fixed to ring 2 [$x_{1,2}, y_{1,2}$ and $z_{1,2} = z$ are the azimuthal (increasing in the beam direction), radial and vertical coordinates respectively]. If we then assume that, in their respective frames, the density distributions in the x, y and z directions are decoupled and furthermore independent of x_1, x_2 , respectively, we have:

$$n'_{1,2}(x_{1,2}, y_{1,2}, z_{1,2}) = n'_{1,2}(y_{1,2}, z) = T_{1,2}(y_{1,2}) S_{1,2}(z) \quad (47)$$

Furthermore we have then for the currents I_1 and I_2 in the rings:

$$\frac{N_{S_{1,2}}}{2\pi R} = \frac{I_{1,2}}{ec} = \int n'_{1,2}(y_{1,2}, z) dy_{1,2} dz \quad (48)$$

We then obtain an expression for h_{eff} by substituting Eq. (48) into Eq. (46), taken e.g. in the frame x_1, y_1, z of ring 1, and transforming the volume element in this frame to that in the y_2, y_1, z frame by means of the transformation

$$y_2 = x_1 \sin \alpha - y_1 \cos \alpha ; \quad y_1 = y_1 ; \quad z = z \quad (49)$$

from which it follows that

$$dx_1 dy_1 dz = \frac{\partial(x_1, y_1, z)}{\partial(y_2, y_1, z)} dy_2 dy_1 dz \quad (50)$$

$$= \frac{1}{\sin \alpha} dy_2 dy_1 dz \quad (51)$$

The result is

$$\frac{1}{h_{\text{eff}}} = \frac{e^2 c^2}{I_1 I_2} \int h'_1(y_1, z) h'_2(y_2, z) dy_1 dy_2 dz \quad (52)$$

$$= \frac{\int h'_1(y_1, z) h'_2(y_2, z) dy_1 dy_2 dz}{\int h'_1(y_1, z) dy_1 dz \int h'_2(y_2, z) dy_2 dz} \quad (53)$$

$$= \frac{\int S_1(z) S_2(z) dz}{\int S_1(z) dz \int S_2(z) dz} \quad (54)$$

Equation (54) is equal to Eq. (1) of Ref. 9 and Eq. (2) of Ref. 10 and hence the overlap integral in Eq. (54) can indeed be obtained from the measurement of h_{eff} by these methods. Substituting the expression for h_{eff} [Eq. (53)] into the expression for the monitorate [Eq. (44)], one has, with Eqs. (51) and Eq. (48):

$$R_M(\theta) = \frac{c}{h_{\text{eff}} \operatorname{tg} \frac{\alpha}{2}} \left(\frac{N_{S_1}}{2\pi R} \right) \left(\frac{N_{S_2}}{2\pi R} \right) \frac{d\sigma_c}{d\Omega} \Delta \Omega_M \quad (55)$$

$$\equiv L_{\text{eff}} \frac{d\sigma_c}{d\Omega} \Delta \Omega_M \quad (56)$$

which defines the effective luminosity L_{eff} , by comparison with Eq. (9).

3) The differential overlap function $n_1(x, y, z) n_2(x, y, z)$ is obtained by differentiation of Eq. (44); with Eqs. (47) and (51) we have

$$\frac{d^2 R_M(\theta)}{dy_1 dy_2} dy_1 dy_2 = \frac{c}{\operatorname{tg} \frac{\alpha}{2}} \frac{d\sigma_c(\theta)}{d\Omega} \Delta \Omega_y T_1(y_1) T_2(y_2) dy_1 dy_2 \int S_1(z) S_2(z) dz \quad (57)$$

and

$$\frac{dR_M(\theta)}{dz} dz = \frac{c}{\operatorname{tg} \frac{\alpha}{2}} \frac{d\sigma_c(\theta)}{d\Omega} \Delta \Omega_z S_1(z) S_2(z) dz \int T_1(y_1) T_2(y_2) dy_1 dy_2 \quad (58)$$

Here $\Delta \Omega_y$ and $\Delta \Omega_z$ are the solid angles of the respective monitor hodoscopes.

By combining Eqs. (57) and (58) and using Eqs. (47) and (55) one finds

$$h_1'(y_1, z) h_2'(y_2, z) dy_1 dy_2 dz =$$

$$\frac{I_1 I_2}{e^2 c^2 k_{eff}} \left(\frac{1}{\Delta \mathcal{R}_y} \frac{d^2 R_{11}(\theta)}{dy_1 dy_2} \right) \left(\frac{1}{\Delta \mathcal{R}_z} \frac{dR_{11}(\theta)}{dz} \right) \left(\frac{\Delta \mathcal{R}_{11}}{R_{11}(\theta)} \right)^2 dy_1 dy_2 dz \quad (59)$$

Returning now to the cartesian frame x, y, z and using the Jacobian in Eq. (50), Eq. (59) becomes

$$h_1(x, y, z) h_2(x, y, z) dx dy dz =$$

$$\frac{I_1 I_2 \sin \alpha}{e^2 c^2 k_{eff}} \left(\frac{1}{\Delta \mathcal{R}_y} \frac{d^2 R_{11}(\theta)}{dy_1 dy_2} \right) \left(\frac{1}{\Delta \mathcal{R}_z} \frac{dR_{11}(\theta)}{dz} \right) \left(\frac{\Delta \mathcal{R}_{11}}{R_{11}(\theta)} \right)^2 dx dy dz \quad (60)$$

which is the quantity to be substituted into Eq. (43) for the rate in the spectrometers.

In practice the three functions (integral monitor, h_{eff} measurement, differential monitors in y_1 , y_2 and z direction) are performed by two sets of counters and spark chambers, one in the horizontal plane, one in the vertical plane. It is clear from the formulae above that the monitors must satisfy the requirements that their solid angle is independent of x, y, z and that the scattering angle ϑ is the same for both monitors. This is obtained by placing trigger counters and spark chambers close to the intersection at $\sim 90^\circ$ in the median plane and above (or below) the intersection. The counters and chambers in the median plane are part of the large angle spectrometer, described in Section 4 (see Fig. 8).

In order to estimate the rate of charged particles, integrated over all momenta, seen by the monitors, we have calculated

$$\frac{dN_c}{d\Omega} = \sum_{\substack{\text{all} \\ \text{charged} \\ \text{particles}}} \int_0^{P_{LIM}} \frac{d^2N}{dp d\Omega} dp \quad (61)$$

at various angles. Here, p_{LIM} is the kinematical limit at the corresponding angle. Figure 19 shows the results for beam-beam interactions and for beam-gas interactions; for the latter the effective beam length is calculated from Eq. (38). For comparison the results for neutrons in beam-beam and beam-gas interactions is also indicated. It is seen that for all cases the intensity is rapidly dropping at small angles; for large angles the distribution flattens out for charged beam-beam interactions while for the other cases the drop continues. In fact at $\sim 90^\circ$ we have

$$\begin{aligned} N_{bb} &\approx 0.4 && \text{charged particles/sr.int. proton} \\ N_{bg} &\approx 0.03 && \text{charged particles/sr.int. proton} \end{aligned} \quad (62)$$

and hence the ratio of the rates for beam-gas and beam-beam interactions at $\sim 90^\circ$ is

$$\frac{I_{bg}}{I_{bb}} = \frac{L_{bg} \times \sigma_{pN_2} \times N_{bg} \times 2}{L_{bb} \times \sigma_{pp} \times N_{bb} \times 2} \approx 2.5 \times 10^{-5} \quad (63)$$

with

$$L_{bg} = \text{Luminosity for beam-gas interactions} = 10^{26} / \text{cm}^2 \cdot \text{sec} \cdot \text{cm beam, see Eq. (33)}$$

$$L_{bb} = \text{Luminosity for beam-beam interactions} = 4 \times 10^{30} / \text{cm}^2 \cdot \text{sec}$$

$$\sigma_{pp} = 30 \text{ mb}$$

$$\sigma_{pN_2} = 380 \text{ mb}$$

The factor 2 arises from the contributions defined with respect to each beam. It is seen from Eq. (63) that a set of chambers and counters placed at $\sim 90^\circ$ measures predominantly beam-beam interactions.

The counting rate in the monitors is limited by solid angle and by a lower limit on the accepted momenta imposed by the precision required for h_{eff} . The uncertainty in the beam profile is mainly due to multiple scattering in the wall of the vacuum box. For particles with $\beta > 0.75$, the multiple scattering is less than 10 mrad, which results in a position determination not worse than 1 mm; this corresponds to an error in h of about 0.5% for Gaussian-type distributions. Hence, a sample of tracks has to be selected, for which the angular acceptance along the direction of the distribution is less than ± 5 mrad around the central angle, whereas in the perpendicular direction the acceptance can be larger, about 100 mrad, within the limits of flatness of the angular distribution. The selection should give rise to a constant $\Delta\Omega$ for each point of the interaction region. For a solid angle $\Delta\Omega = \pi \times 5 \times 100 \text{ msr} = 1.6 \text{ msr}$, and all charged particles above $\beta = 0.75$, i.e. 1.4% of all charged particles, the rate in the monitor is about 1/sec at a luminosity of $4 \times 10^{30} / \text{cm}^2 \cdot \text{sec}$. This rate is quite adequate. As to the measurement of h_{eff} , this is most simply done by a vertical movement of the beam as suggested in Ref. 9. The proposal of Ref. 10 (dropping a wire through the intersecting beams) seems more difficult to realize since it would require movable parts in an environment of 10^{-11} Torr N_2 and in the field of view of the monitors. The profile monitor operates continuously.

The selection of particles with $\beta > 0.75$ can be done with a liquid or glass Čerenkov counter for the monitor in the vertical direction. In the horizontal direction, the monitor is incorporated in the large angle spectrometer. Here, the multiple scattering in the Čerenkov counter would interfere with the operation of the large angle spectrometer, hence time-of-flight selection for particles with $\beta > 0.75$ will be applied here.

A relative monitor, an extension of the absolute monitor, for checking the time stability of the ISR operation, can have a much larger solid angle than the absolute monitor. For $\Delta\Omega = 1 - 100$ msr the rate is $10^2 - 10^4$ /sec at a luminosity of 4×10^{30} /cm². sec.

Table 1

Optical characteristics of the small angle spectrometer

Solid angle	: 0.03 msr
Momentum bite	: $\Delta p/p = \pm 10\%$
Dispersion at focus	: 0.125 (GeV/c)/cm at 25 GeV/c
Chromatic aberration	: Displacement of focal plane 1.67 m/% $\Delta p/p$
Depth of field	: Apparent increase of object size for particles emerging from front (rear) end of intersecting region +(-) 10%
Vertical magnification	: -2
Horizontal magnification	: -1
Limiting apertures	: Horizontally: Septum 1, Septum 2, Q ₄ Vertically : Q ₃
Field gradients required for 25 GeV/c (T/m):	Q ₁ = 9.95 Q ₃ = 8.19 Q ₂ = 8.19 Q ₄ = 9.95
Field in bending magnets for 25 GeV/c (T)	: Septum 1 : 1.77 Septum 2 : 1.77 BM1 = BM2 = BM3 = 1.60
Accuracy in momentum	{ with counters only : ~ 4% with counters + spark chambers : ~ 0.2%
Accuracy in scattering angle	: < 1.5 mrad

Table 2

Electrical characteristics of the small angle spectrometer

	Septum I	Septum II	1.5 m split-pole quadrupole	Standard 2 m quadrupole	Standard 2 m bending magnet
Quantity	1	1	2	2	3
Length (m)	1.5	3.0	1.89	2.46	2.5
Gap (m)	0.06 (H) 0.10 (V)	0.075 (H) 0.30 (V)	0.2 (φ)	0.2 (φ)	0.14 (H) 0.33 (V)
Nominal current (A)	~ 17 kA (for 5 turns)	~ 18 kA (for 6 turns)	875 A	750 A	850 A
Nominal gradient (T/m)	-	-	9.3	1.05	-
Field (T)	1.8	1.8	-	-	1.6
$\int Bdl$ (Tm)	2.7	5.4	-	-	3.48
Total winding resistance (ohm)	$\sim 0.75 \times 10^{-3}$	$\sim 0.5 \times 10^{-3}$	0.36	0.195	0.36
Power (kW)	~ 300	~ 200	300	115	260
Weight (tons)	~ 2.5	~ 20	3	9	25

Table 3

Optical and electrical characteristics of the large angle spectrometer

Peak solid angle	: 6.6 msr
Momentum bite	: 0.8-1.5 GeV/c with $\Delta\Omega > 3$ msr with magnets set for 1 GeV/c
Dispersion	: In the range 0.8-1.5 GeV/c: 0.02 (GeV/c)/cm
Limiting aperture	: Q_2
Field gradients required for 1 GeV/c (T/m)	: $Q_1 = 3.84$ $Q_2 = 2.46$
Field in bending magnet for 1 GeV/c	: 1.2 T
Quadrupoles have non- standard apertures	: 0.35 m \emptyset , 1 m long: power and weight not yet specified
1 m H-type bending magnet	: Length 1.7 m Gap 0.5 m (H) \times 0.2 m (V) [(V) is non-standard]
Nominal current	: 675 A
Field	: ~ 1.3 T (with gap height increased to 0.2 m)
Power	: 93 kW
Weight	: 15 tons

Table 4

Optical and electrical characteristics of
the medium angle spectrometer

Solid angle	: 0.125 msr
Momentum bite	: $\Delta p/p \geq \pm 10\%$
Dispersion at focus	: 0.067 GeV/c/cm
Horizontal magnification	: -1.85
Vertical magnification	: -0.6
Limiting apertures	: Horizontally: Q_2 (exit), Q_3 (entrance) Vertically : Q_4 (centre)
Field gradients required for 10 GeV/c (T/m)	: $Q_1 = 7.63$ $Q_3 = 6.16$ $Q_2 = 6.16$ $Q_4 = 7.63$
Field in BM for 10 GeV/c:	1.60 T
All quadrupoles are of the 1.5 m split-pole type	: See Table 2
The bending magnet is standard	: See Table 2

Table 5

Comparison between vertical and horizontal bending with one septum magnet with a septum of 30 mm thickness. 75 mm height and length l_1 for a production angle $\alpha_0 = 15$ mrad of the secondary particles.

The bending angle, α_1 , in the septum magnet is calculated for 25 GeV/c protons.

The distance between l_1 , the centre of the septum and the entrance of the ISR magnet

is L_1 [from Eq. (22)], $H_{1V} = 15$ mm, $H_{1H} = 45$ mm, from Fig. 17].

Displacement at the entrance of the ISR magnet due to the

production angle is $\alpha_0 L_0 = 0.015 \times 9.8 = 0.147$ m.

The calculated power is for the septum only.

The space for a second element is $l_{2V(H)}$ [Eq. (23)].

Septum	l_1 (m)	α_0 (mrad)	L_{1V} (m)	L_{1H} (m)	$\alpha_0 L_0 + \alpha_1 L_{1V}$ (m)	$\alpha_0 L_0 + \alpha_1 L_{1H}$ (m)	W_1 (kW)	l_{2V} (m)	l_{2H} (m)
A	3	64	5.3	3.8	0.486	0.359	345	2.8	0.8
B	4	85	4.8	2.8	0.555	0.385	460	1.8	-
C	5	107	4.3	2.3	0.607	0.393	575	0.8	-
D	6	128	3.8	1.8	0.633	0.377	690	-	-

Table 6

Septum magnet system for vertical bending. First septum at maximum conditions for d_1 and l_1 in order to obtain $B_1 = 1.8$ T. Bending angles for $p = 25$ GeV/c. The obstacle to be cleared has $H = 0.61$ m. Hence, for $\alpha_0 = 15$ mrad and $l_0 = 9.8$ m, $\alpha_1 l_1 + \alpha_2 l_2 \geq 0.463$ m. Distance of first septum to median plane is $H_1 = 15$ mm (see Fig. 17), for second septum H_2 is chosen to be 44 mm. The length, l_2 of the second septum is adjusted to the requirement for $\alpha_2 l_2$.

Septum system	d_1 mm	l_1 m	α_1 mrad	L_1 m	$\alpha_1 L_1$ m	W_1 (60) kW	d_2 mm	l_2 m	α_2 mrad	L_2 m	W_2 (75) kW	W_{total} kW	l_Q m
a	24.0	2.0	43.5	6.2	0.270	450	98	2.2	47	0.170	80	530	1.5
b	17.5	1.5	32.5	6.85	0.223	370	60	2.6	55.5	0.240	150	520	2.0
c	15.5	1.0	21.5	7.3	0.153	290	30	3.0	64	0.310	345	635	2.3
d	12.5	0.5	10.5	7.75	0.081	175	6 \rightarrow $B_2 < 1.8$ T	-	-	-	-	-	-
e	11.5	0.25	5.5	7.93	0.044	84	-	-	-	-	-	-	-
D ^{††}	30.0	6.0	128.0	3.8	0.486	-	-	-	-	-	-	690	-

*) For septum of 60 mm distance between the poles } sizes determined from phase space requirements.
 **) For septum of 75 mm distance between the poles }
 †) Distance available for Q magnet, calculated with formula analogous to Eq. (23).
 ††) For comparison; taken from Table 5.

Table 7

Optimized septum magnet system for vertical bending

Septum	1	2	
d	0.02	0.06	m
h	0.06	0.075	m
l	1.5	3.0	m
B	1.8	1.8	T
Bl	2.7	5.4	Tm
α	32	64	mrad
nI	86	107	kA turn
W_s	248	172	kW
W_t	300	206	kW
p_B	13	13	kg/cm ²
d_s	2.3	8.8	mm
S	6450	4500	kg/cm ²

d, h, l thickness, height, length of septum

B field

Bl bending strength

$\alpha = Bl/3.336 p$ for particles of $p = 25 \text{ GeV}/c$

nI ampere turns

W_s power dissipated in septum

$W_t \approx 1.2 W_s$ total power dissipated, including return winding, etc.

p_B magnetic pressure

d_s thickness of stainless steel plate for support of the septum

S stress on stainless steel plate

Table 8

Rates per day in the small angle spectrometer
 Optical characteristics in Table 1; ISR luminosity = $4 \times 10^{30} / \text{cm}^2 \cdot \text{sec}$; vacuum 10^{-11} Torr N_2
 bb, bg = rates, resulting from beam-beam, beam-gas interactions, respectively.

p (GeV/c)	θ prod mrad	20			15			10			5			2.5			0.25		
		bb	bg	bg/bb %	bb	bg	bg/bb %	bb	bg	bg/bb %	bb	bg	bg/bb %	bb	bg	bg/bb %	bb	bg	bg/bb %
25	π^+	1.8+4	3.4+2	1.9	3.3+5	7.4+3	2.3	7.8+5	2.0+4	2.5	7.2+5	1.5+4	2.1	4.0+5	6.2+3	1.6	8.4+3	1.0+2	1.1
	150	5.2-5	-	-	1.2+0	6.0-3	0.5	1.8+3	2.5+1	1.4	7.2+4	9.0+2	1.3	2.0+5	2.7+3	1.3	3.4+3	5.2+1	0.6
25	K^+	2.7+3	1.7+1	0.6	2.9+4	4.8+2	1.6	1.0+5	1.8+3	1.8	1.0+5	2.0+3	2.0	6.0+4	9.0+2	1.5	6.6+2	1.0+0	1.4
	150	4.0-4	-	-	1.8+0	6.6-3	0.4	3.6+2	4.0+0	1.1	1.6+4	1.9+2	1.1	4.0+4	3.4+2	0.9	6.6+2	4.0-1	0.06
25	p	2.4+6	9.0+4	3.7	2.1+6	6.2+4	3.0	8.4+5	2.3+4	2.7	7.8+4	3.0+3	3.9	8.4+3	6.7+2	7.9	1.2+1	1.4+1	117.0
	150	9.0-1	-	-	7.8+1	1.9+0	2.4	2.8+3	7.8+1	2.8	1.4+4	6.0+2	4.3	6.0+3	4.4+2	7.4	1.2+1	7.2+0	60.0
25	π^-	5.0+3	4.4+1	0.9	7.8+4	1.0+3	1.2	2.4+5	2.6+3	1.1	4.1+5	2.3+3	0.6	3.4+5	1.2+3	0.3	9.0+3	1.8+1	0.2
	150	2.1-5	-	-	4.8+0	7.2-4	0.02	9.0+2	3.4+0	0.4	5.2+4	1.4+2	2.7	1.6+5	4.4+2	0.3	9.0+3	1.0+1	0.1
25	K^-	4.8+1	1.5+0	3.1	1.0+3	4.4+1	4.4	7.2+3	2.5+2	3.5	4.1+4	5.7+2	1.4	6.6+4	3.3+2	0.5	1.1+3	1.3-1	0.01
	150	2.0-4	-	-	1.2+0	2.5-4	0.02	1.8+2	1.1+0	0.6	1.2+4	6.6+1	0.6	4.6+4	1.4+2	0.3	1.1+3	4.9-2	4.0-3
25	\bar{p}	3.0+0	3.7-2	1.2	1.8+2	7.3+0	4.1	1.4+3	4.4+1	3.1	7.2+3	5.1+1	0.7	1.0+4	1.4+1	0.1	4.5+1	1.4-6	3.0-4
	150	7.8-6	-	-	6.0-1	1.6-4	0.03	6.0+1	2.5-1	0.4	2.7+3	7.2+0	0.3	7.2+3	7.2+0	0.1	4.5+1	-	-

Table 9

Rates per day in the large angle spectrometer
Optical characteristics in Table 3; ISR luminosity = $4 \times 10^{30}/\text{cm}^2 \cdot \text{sec}$; vacuum 10^{-11} Torr N_2
bb, bg = rates, resulting from beam-beam, beam-gas interactions, respectively.

p (GeV/c)	$\phi_{\text{prod}} / \text{mrad}$	3.0			2.5			2.0			1.5			1.0			0.5			0.25		
		bb	bg	bg/bb %	bb	bg	bg/bb %	bb	bg	bg/bb %	bb	bg	bg/bb %	bb	bg	bg/bb %	bb	bg	bg/bb %	bb	bg	bg/bb %
1000+1880	π^+	2.4+2	-	-	2.6+3	-	-	2.6+4	-	-	2.2+5	2.6+1	0.01	1.2+6	2.0+2	0.02	3.0+6	2.0+4	0.7	2.0+6	1.1+4	0.5
	1440	2.6+2	-	-	2.6+3	-	-	2.2+4	-	-	1.5+5	-	-	7.2+5	-	-	1.9+6	6.8+3	0.3	1.6+6	9.0+3	0.6
1000+1880	K^+	4.0+2	-	-	4.1+3	-	-	9.6+4	-	-	2.8+5	9.0-1	3.0-4	1.1+6	1.0+2	0.01	1.3+6	4.6+2	0.04	1.6+5	1.1+2	0.07
	1440	3.0+2	-	-	2.6+3	-	-	2.0+4	-	-	1.4+5	-	-	6.2+5	-	-	9.8+5	6.0+1	0.06	1.5+5	6.0+1	0.04
1000+1880	p	4.6+2	-	-	3.4+3	-	-	1.9+4	-	-	7.0+4	-	-	1.1+5	4.6+3	4.2	4.0+4	1.0+4	25.0	3.4+3	2.2+3	65.0
	1440	5.0+2	-	-	3.8+3	-	-	1.9+4	-	-	6.0+4	-	-	9.6+4	-	-	3.8+4	-	-	3.4+3	-	-
1000+1880	π^-	1.6+2	-	-	1.9+3	-	-	2.0+4	-	-	1.8+5	2.0-1	1.0-4	1.2+6	2.1+2	0.02	3.4+6	2.2+3	0.06	2.6+6	2.0+3	0.08
	1440	1.7+2	-	-	1.9+3	-	-	1.8+4	-	-	1.4+5	-	-	7.6+5	-	-	2.2+6	4.4+2	0.02	1.9+6	1.3+3	0.07
1000+1880	K^-	4.1+2	-	-	4.8+3	-	-	6.0+4	-	-	4.0+5	1.1-2	3.0-6	1.7+6	1.0+0	6.0-5	2.0+6	3.0+0	2.0-4	2.6+5	4.9+0	2.0-3
	1440	3.0+2	-	-	3.0+3	-	-	2.8+4	-	-	2.0+5	-	-	9.4+5	-	-	1.6+6	2.4+0	2.0-4	2.4+5	3.0+0	1.0-3
1000+1880	\bar{p}	3.6+2	-	-	3.0+3	-	-	2.0+4	-	-	1.0+5	-	-	2.6+5	-	-	1.5+5	-	-	1.4+4	-	-
	1440	2.0+2	-	-	1.7+3	-	-	1.2+4	-	-	6.6+4	-	-	2.0+5	-	-	1.4+5	-	-	1.4+4	-	-

Table 10

Rates per day in the medium angle spectrometer
 Optical characteristics in Table 4; ISR luminosity = $4 \times 10^{30} / \text{cm}^2 \cdot \text{sec}$; vacuum 10^{-11} Torr N₂
 bb, bg = rates, resulting from beam-beam, beam-gas interactions, respectively.

p (GeV/c)	θ prod mrad	15				10				5				2.5				0.25			
		bb	bg	bg/bb %	bb	bg	bg/bb %	bb	bg	bg/bb %	bb	bg	bg/bb %	bb	bg	bg/bb %	bb	bg	bg/bb %		
150	π^+	5.0+1	4.5-2	0.9	7.5+3	1.9+2	2.5	3.0+5	6.8+3	2.3	8.5+5	2.1+4	2.5	3.5+4	4.0+2	1.1	5.0+1	4.0+2	1.1		
1000+1880		-	-	-	-	-	-	1.4-4	-	-	3.4+1	-	-	2.8+4	1.4+2	0.5	5.0+1	1.4+2	0.5		
150	K^+	8.0+0	4.9-2	0.6	1.5+3	3.0+1	2.0	6.7+4	1.4+3	2.1	1.7+5	2.6+3	1.5	2.7+3	3.0+0	0.1	5.0+1	3.0+0	0.1		
1000+1880		-	-	-	-	-	-	7.6-4	-	-	8.0+1	-	-	5.0+3	1.4+0	0.03	5.0+1	1.4+0	0.03		
150	p	3.2+2	1.4+1	4.4	1.2+4	6.0+2	5.0	5.7+4	4.5+3	7.9	2.5+4	3.4+3	14.0	5.0+1	5.7+1	114.0	5.0+1	5.7+1	114.0		
1000+1880		2.0-7	-	-	8.6-5	-	-	5.2-4	-	-	4.4+1	-	-	1.1+2	2.8+1	25.0	1.1+2	2.8+1	25.0		
150	π^-	2.0+1	5.7-3	0.03	3.7+3	2.6+1	0.7	2.1+5	1.0+3	0.5	6.7+5	3.4+3	0.5	3.7+4	7.6+1	0.2	3.7+4	7.6+1	0.2		
1000+1880		-	-	-	-	-	-	6.6-5	-	-	2.4+1	-	-	3.2+4	2.5+1	0.8	3.2+4	2.5+1	0.8		
150	K^-	5.0+0	1.9-3	0.4	7.0+2	8.5+0	1.2	5.0+4	4.9+2	1.0	1.9+5	1.0+3	0.5	4.8+3	3.8-1	0.01	4.8+3	3.8-1	0.01		
1000+1880		-	-	-	-	-	-	5.2-4	-	-	9.4+1	-	-	8.6+3	6.2-2	1.0-3	8.6+3	6.2-2	1.0-3		
150	\bar{p}	3.0+0	1.2-3	0.04	2.5+2	1.9+0	0.8	1.1+4	5.7+1	0.5	3.0+4	5.7+1	0.2	1.9+2	-	-	1.9+2	-	-		
1000+1880		-	-	-	-	-	-	3.6-4	-	-	4.0+1	-	-	4.4+2	-	-	4.4+2	-	-		

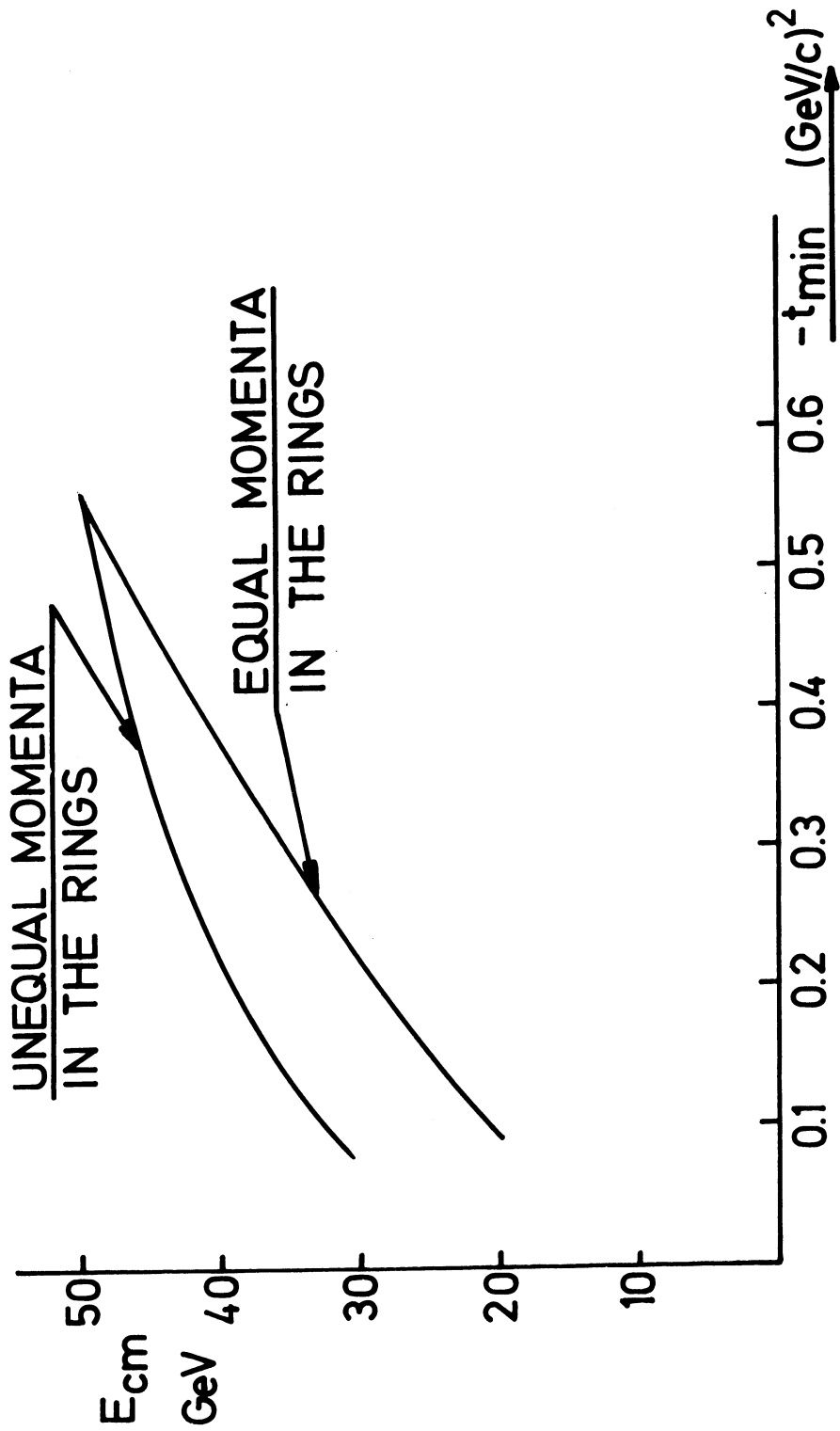
REFERENCES

- 1) The Design Study of Intersecting Storage Rings (ISR) for the CERN Proton Synchrotron, AR/Int. SG/64-9, 12 May 1964, p.88.
- 2) L.W. Jones, Proc. Int. Conf. on High-Energy Accelerators, CERN 1959, p.15. W.C. Middelkoop and A. Schoch, CERN report AR/Int. SG/63-40.
- 3) See, for example, P. Strolin, Properties of stacked proton beams in the ISR, ISR User's Meeting, June 1968.
- 4) M.A. Green, UCRL-16309, August 1965.
- 5) A.M. Wetherell, ISR User's Meeting, June 1968.
- 6) R. Hagedorn and J. Ranft, Momentum spectra of particles produced in pp collisions, preprint CERN-TH/851 (December 1967).
- 7) J. Ranft, Two computer programmes to calculate and test secondary particle yields according to various formulae (CERN Programme Library Nos. W129, W130) CERN-PS/6168-20 Oct. 1967.
- 8) S. Andersson and C. Daum, The production of stable particles, ISR User's Meeting, June 1968.
- 9) S. Van der Meer, Internal Report ISR-PO/68-31, 18 June 1968.
- 10) P. Darriulat and C. Rubbia, On beam monitoring for ISR experiments, ISR User's Meeting, June 1968.

Figure captions

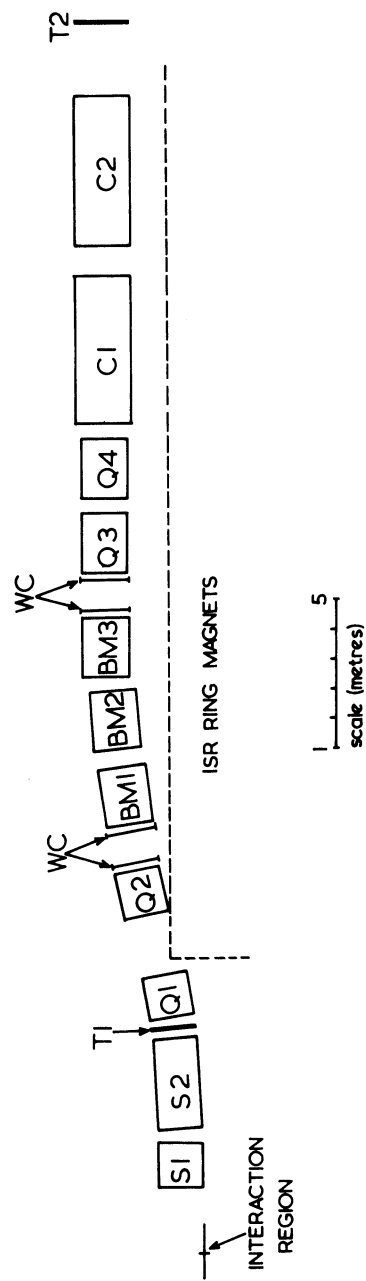
- Fig. 1 : Minimum detectable momentum transfer squared as a function of c.m. energy, for equal and for maximally unequal momenta in the rings.
- Fig. 2 : Small angle spectrometer. Side view of the experimental layout.
- Fig. 3 : Small angle spectrometer. Deflection in the septa and the bending magnets for a secondary produced at 20 mrad.
- Fig. 4 : Small angle spectrometer. Horizontal and vertical ray diagram for a particle leaving the centre of the interacting region. Divergence 4 mrad.
- Fig. 5 : Small angle spectrometer. Horizontal and vertical ray diagram for a particle leaving the front and rear end of the intersecting region (60 cm apart). Divergence 4 mrad.
- Fig. 6A : Small angle spectrometer. Phase space in the vertical (bending) plane at the intersecting region, seen by the spectrometer.
- 6B : Small angle spectrometer. Phase space in the vertical (bending) plane at the focus.
- Fig. 7A : Small angle spectrometer. Phase space in the horizontal plane at the intersecting region seen by the spectrometer.
- 7B : Small angle spectrometer. Phase space in the horizontal plane at the focus.
- Fig. 8 : Large angle spectrometer. Experimental layout.
- Fig. 9 : Large angle spectrometer. Solid angle versus momentum with the bending magnet set for 1 GeV/c.
- Fig. 10A : Large angle spectrometer. Phase space in the horizontal plane at the intersecting region, seen by the spectrometer.
- 10B : Large angle spectrometer. Phase space in the horizontal plane at 1.25 m behind the bending magnet.

- Fig. 11 : Medium angle spectrometer. Experimental layout.
- Fig. 12 : Medium angle spectrometer. Horizontal and vertical ray diagram; divergence 6 mrad.
- Fig. 13A : Medium angle spectrometer. Phase space in the horizontal plane at the intersecting region for particles with 9, 10 and 11 GeV/c momentum, seen by the spectrometer.
- 13B : Medium angle spectrometer. Phase space in the horizontal plane at the focus.
- Fig. 14 : Čerenkov counter threshold curves for various gases and various lengths of the counter, calculated from Eqs. (18) and (19). The solid line indicates the pressure limit, for which K or p does not produce Čerenkov light, as a function of momentum. (For isobutane, the critical temperature is 134°C; at room temperature, condensation sets in at $\sim 2 \text{ kg/cm}^2$.)
- Fig. 15 : Schematic layout of vacuum chamber.
- Fig. 16 : Schematic layout of septum magnets for explanation of formulae (21) to (25).
- Fig. 17 : Schematic drawing of arrangement of beam, wall of vacuum chamber and septum magnet, displaying smallest distance between septum and median plane for vertical and horizontal bending.
- Fig. 18 : Schematic front view of first downstream ISR magnet with endpoints of particle trajectories for some septum magnets, which deflect particles, produced at 15 mrad, away from the circulating beam.
- Fig. 19 : Rates integrated over momentum at fixed angle for beam-beam and beam-gas interactions.



MINIMUM DETECTABLE t IN $PP \rightarrow PP$
FOR $\theta_{LAB} \geq 30$ mrad V.S TOTAL ENERGY

Fig. 1



- T1, T2 : TRIGGERING COUNTERS.
- WC : WIRE CHAMBERS.
- S1, S2. : SEPTUM MAGNETS.
- Q1-4 : QUADRUPOLES.
- BM1-3 : BENDING MAGNETS.
- C1, C2 : CERENKOV COUNTERS.

EXPERIMENTAL LAYOUT (SMALL ANGLES)

Fig. 2

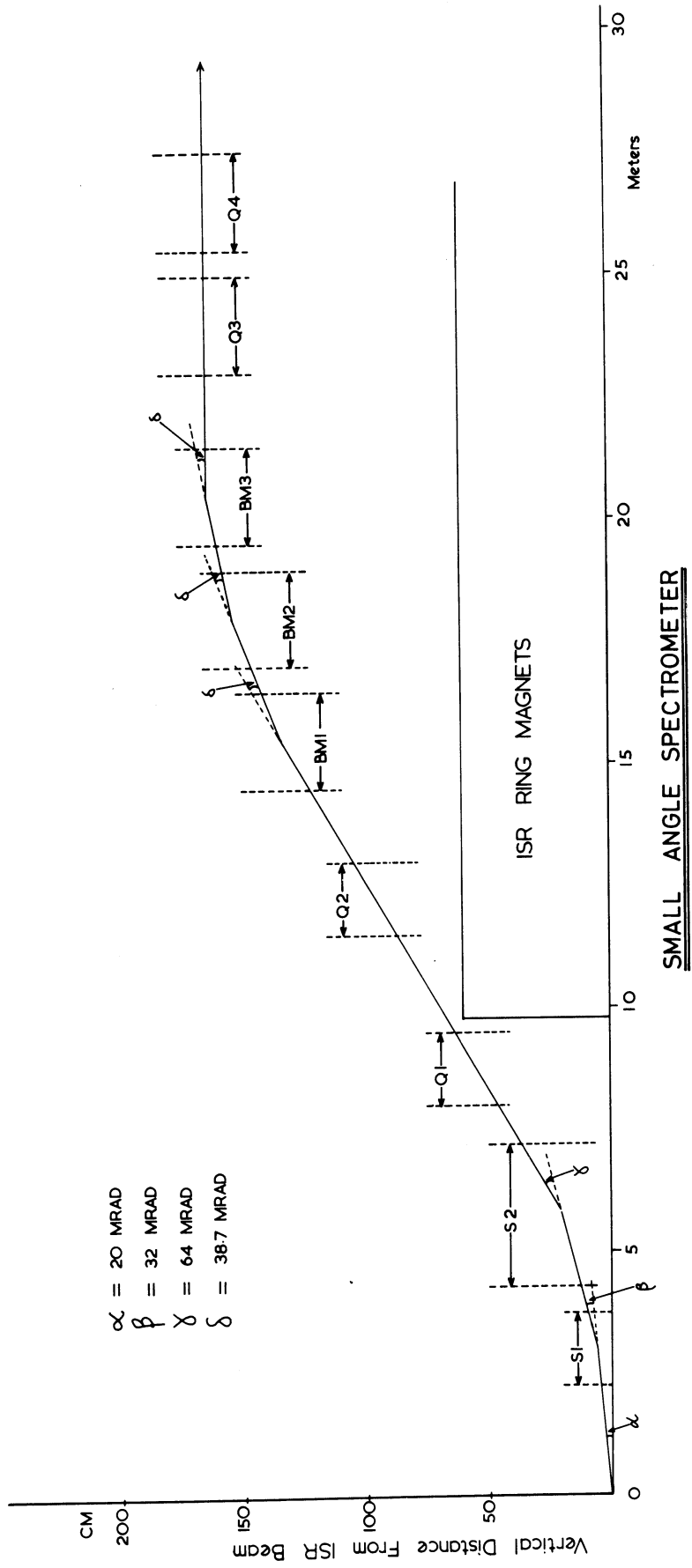
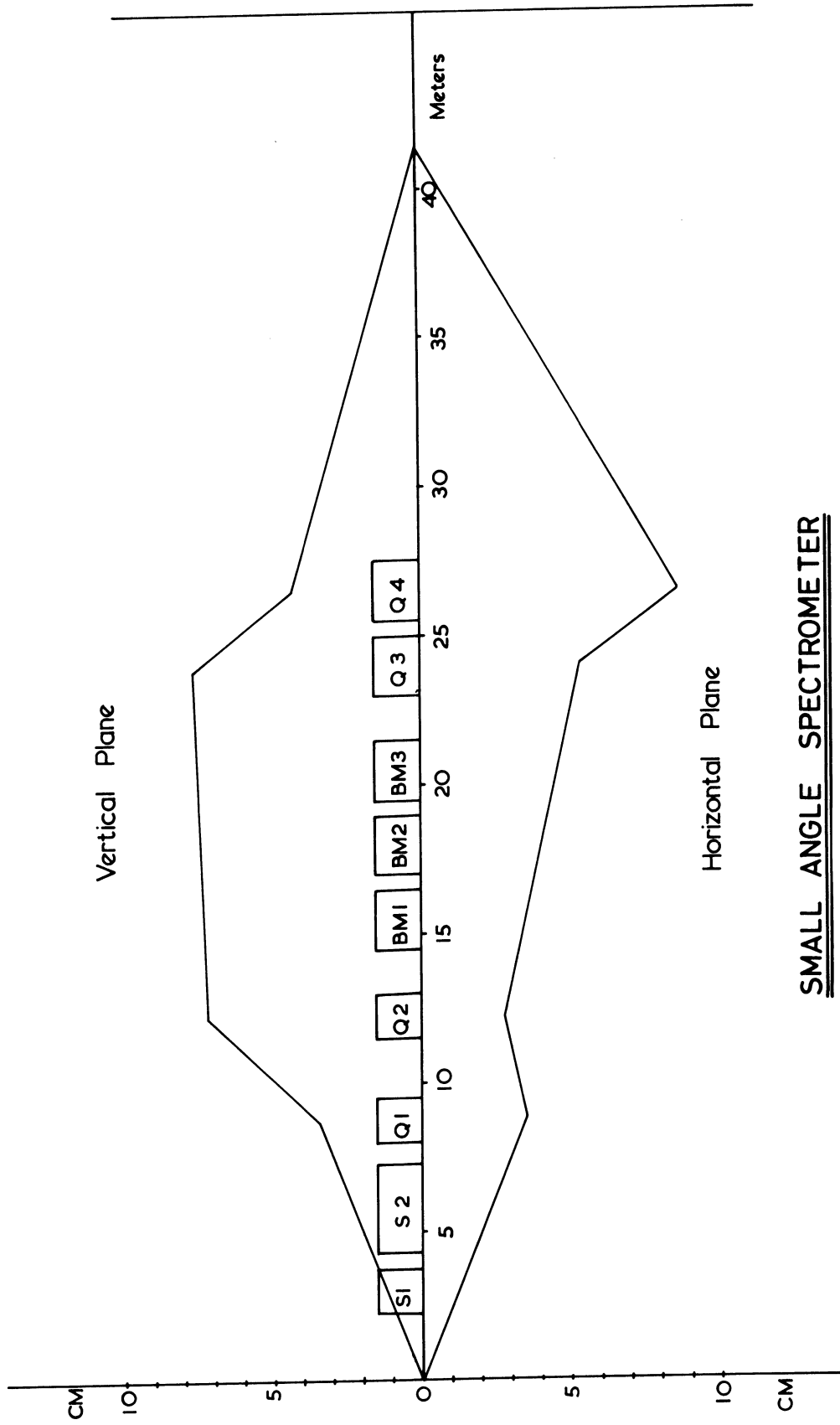


Fig. 3



SMALL ANGLE SPECTROMETER

Fig. 4

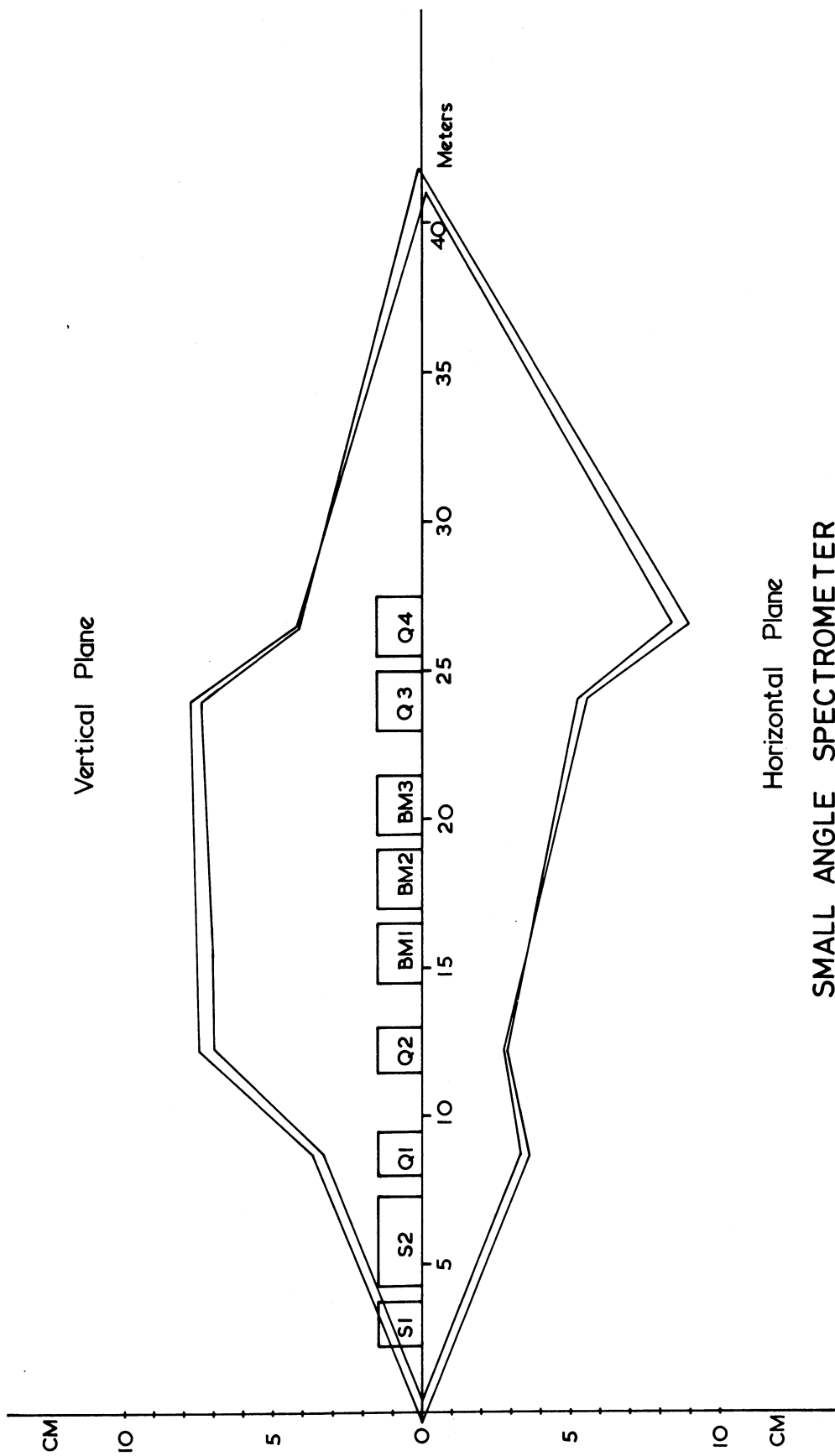


Fig. 5

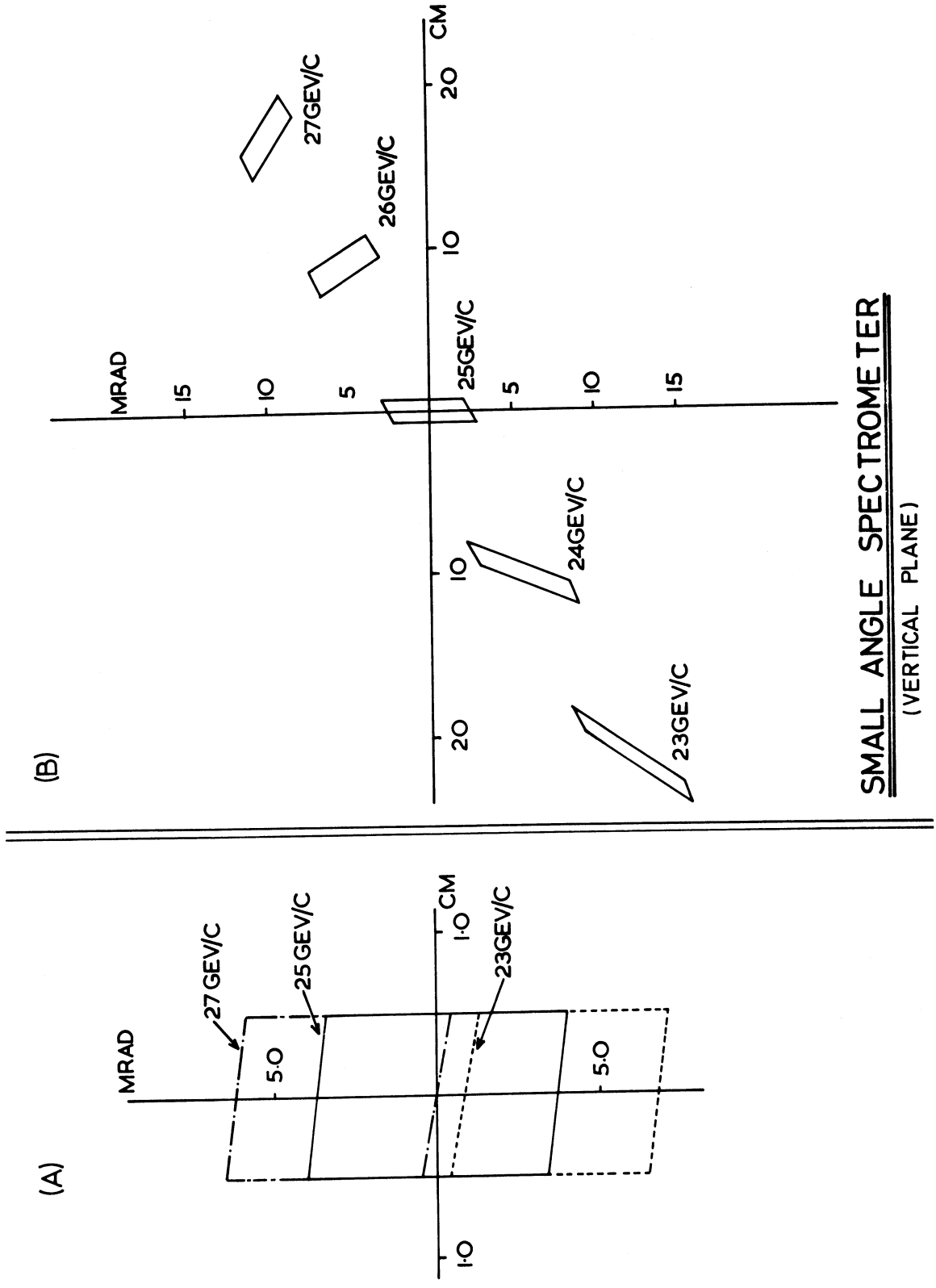
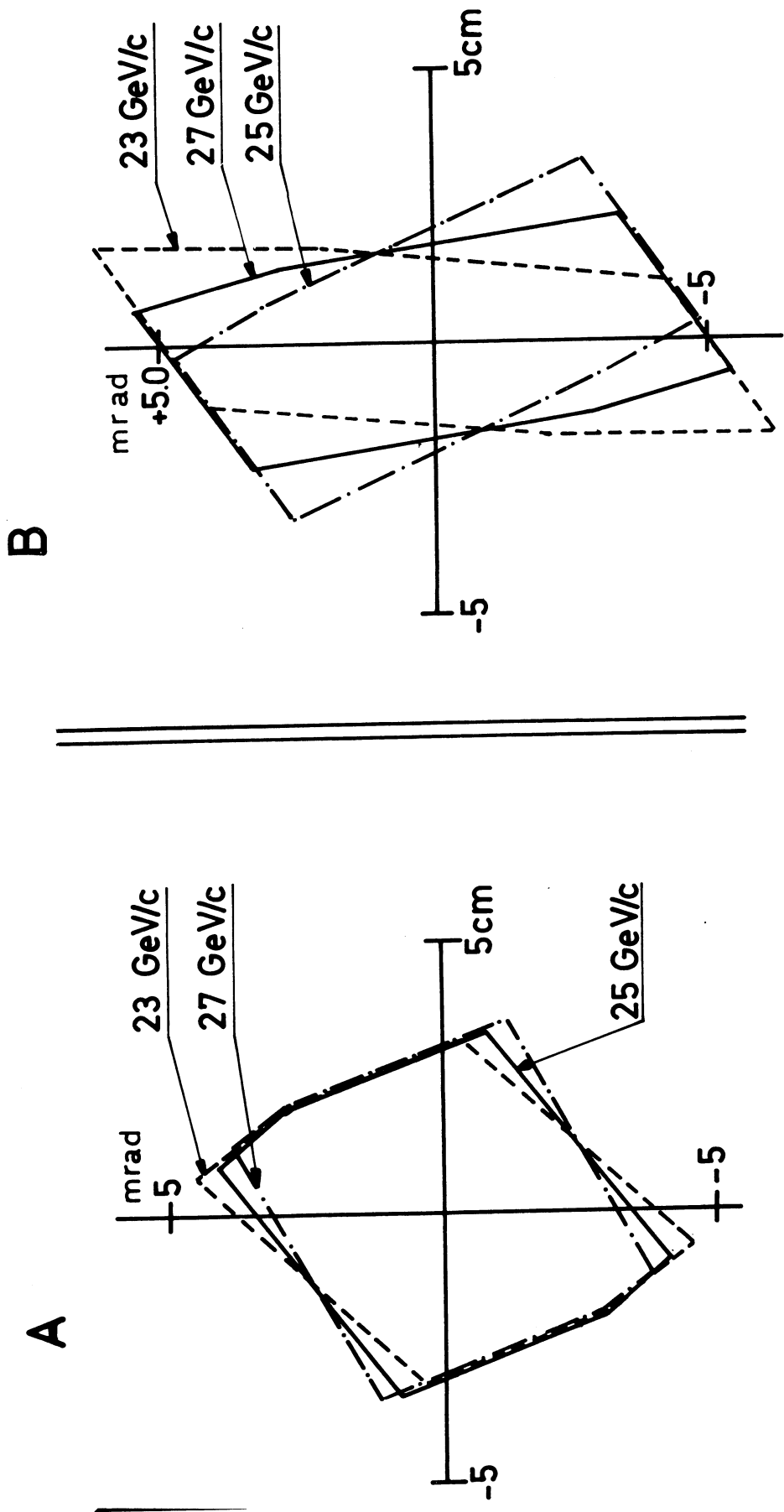


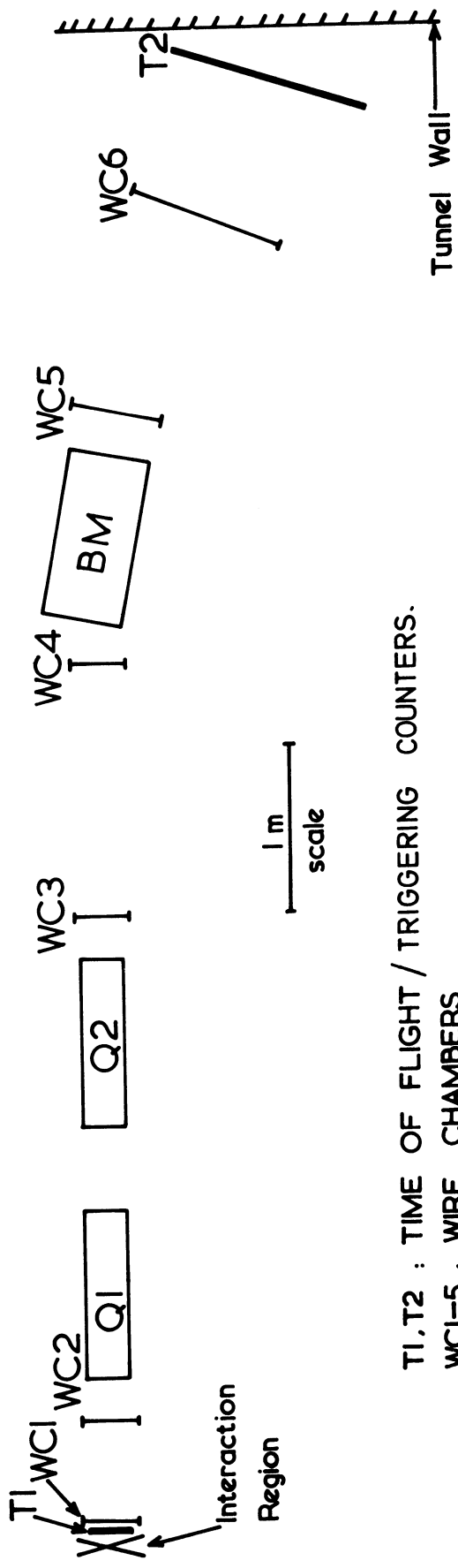
Fig. 6



SMALL ANGLE SPECTROMETER

(HORIZONTAL PLANE)

Fig. 7



T1, T2 : TIME OF FLIGHT / TRIGGERING COUNTERS.

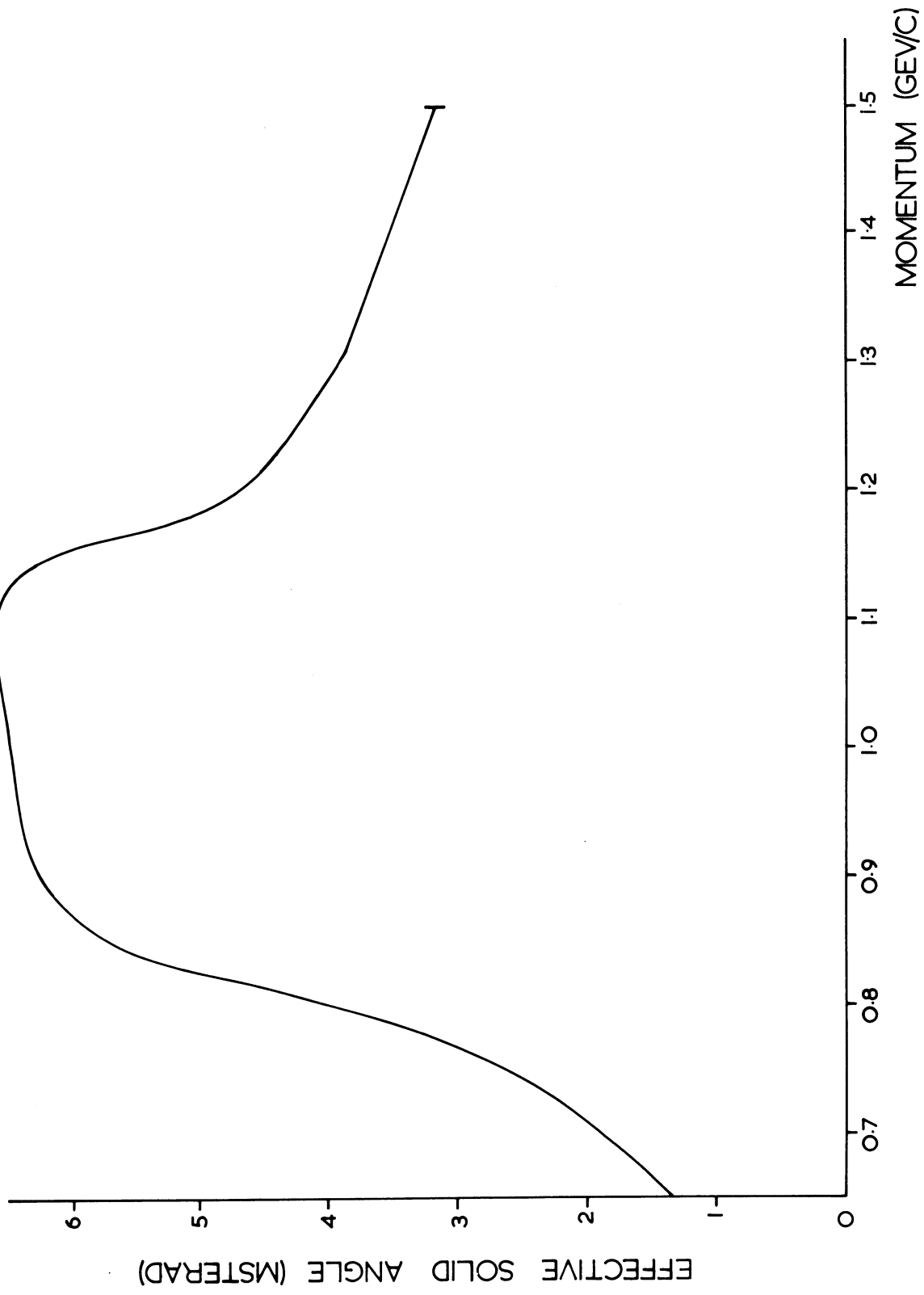
WC1-5 : WIRE CHAMBERS.

Q1, Q2: QUADRUPOLES.

BM : BENDING MAGNET.

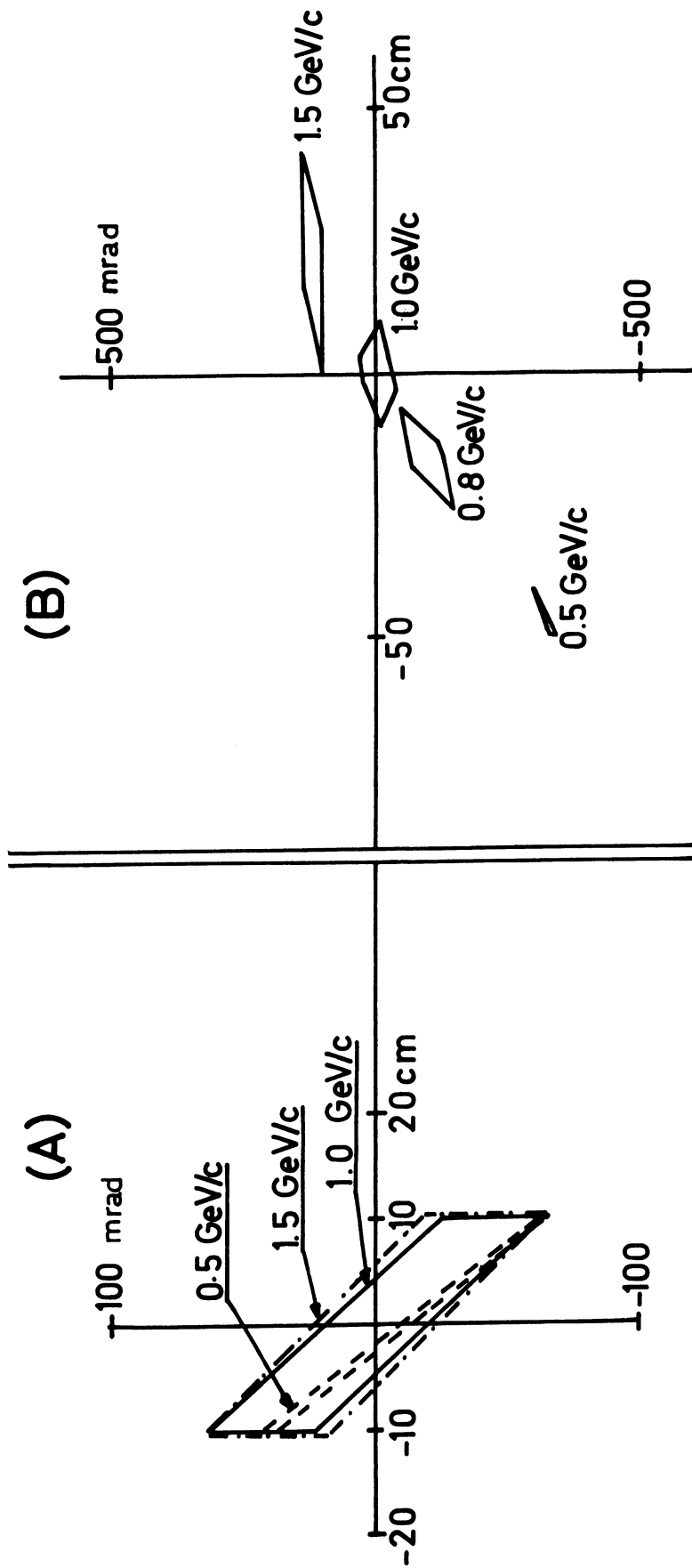
EXPERIMENTAL LAYOUT (LARGE ANGLES)

Fig. 8



LARGE ANGLE SPECTROMETER

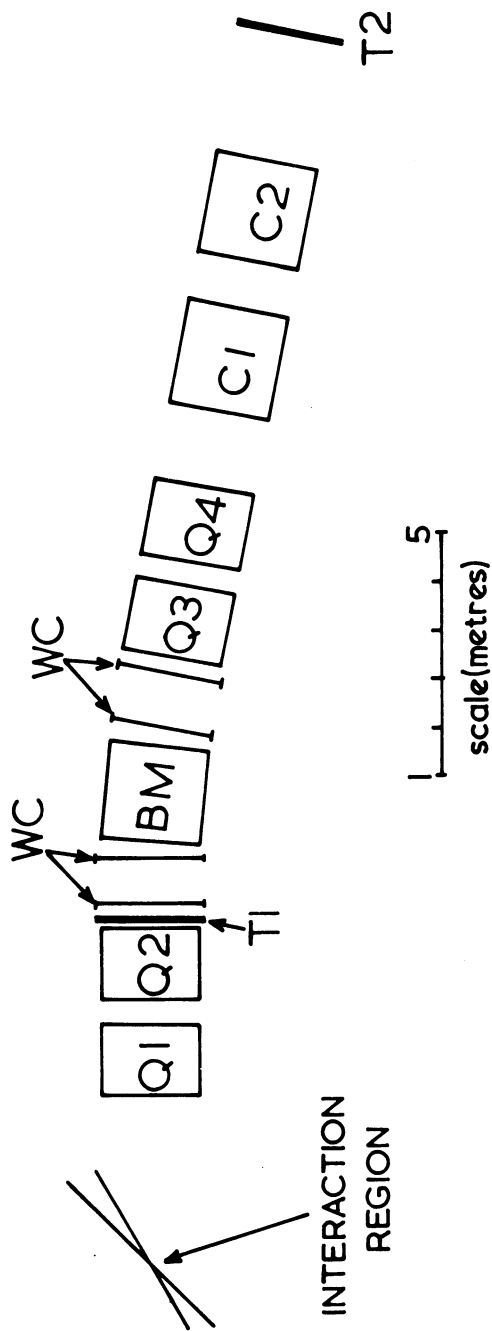
Fig. 9



LARGE ANGLE SPECTROMETER

(HORIZONTAL PLANE)

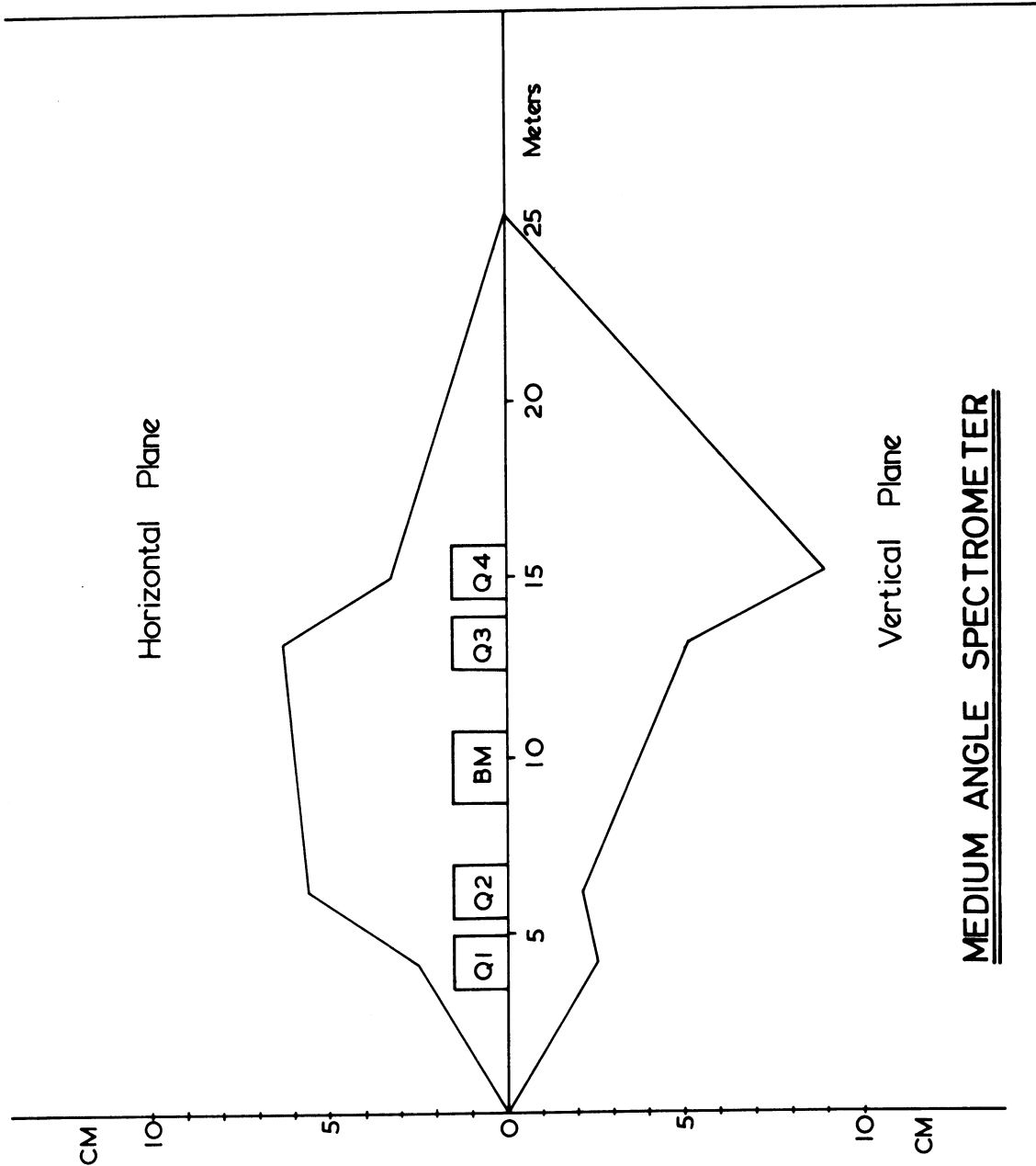
Fig.10



- T1, T2 : TRIGGERING COUNTERS.
- WC : WIRE CHAMBERS.
- Q1-4 : QUADRUPOLES.
- BM : BENDING MAGNET.
- C1, C2 : CERENKOV COUNTERS.

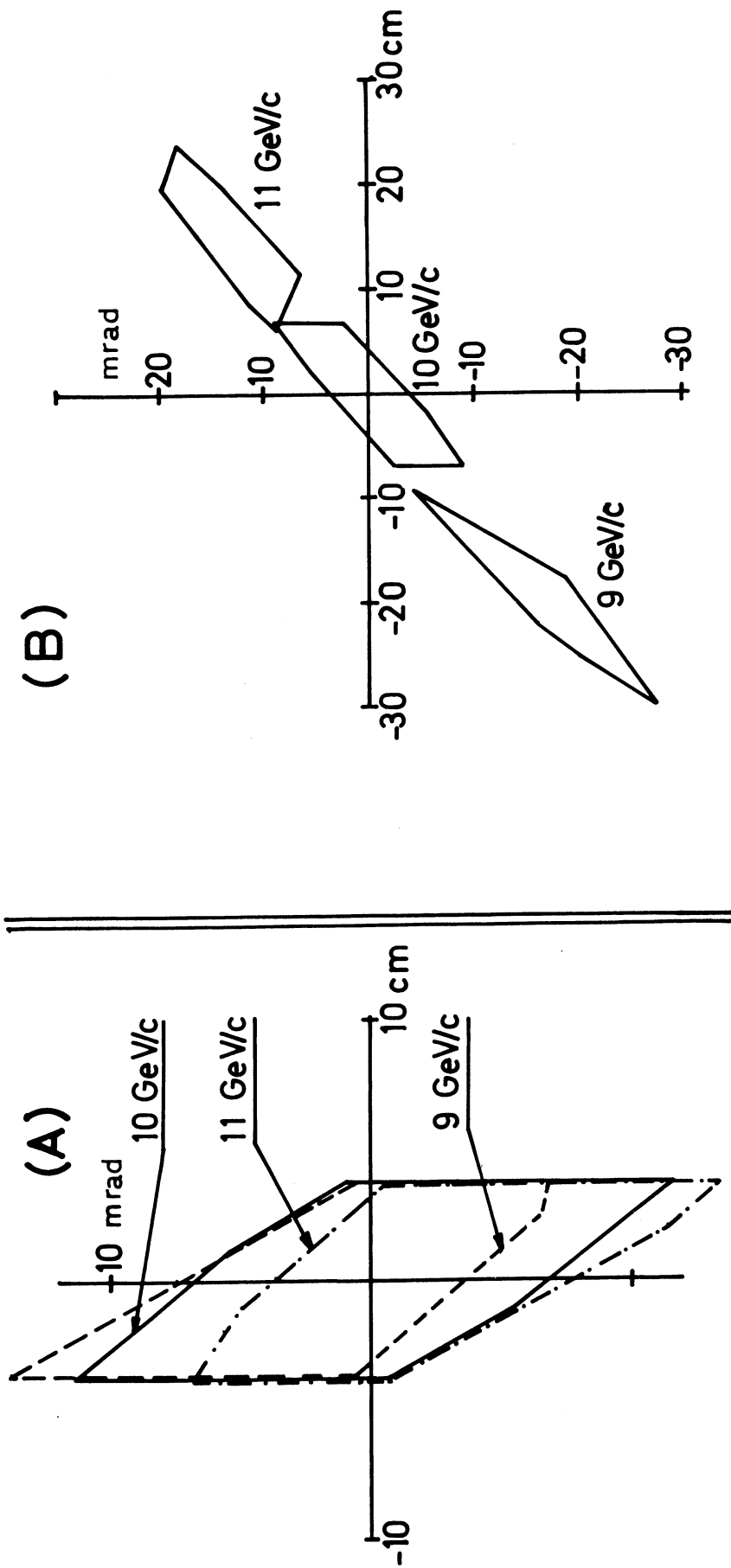
EXPERIMENTAL LAYOUT (MEDIUM ANGLES)

Fig. 11



MEDIUM ANGLE SPECTROMETER

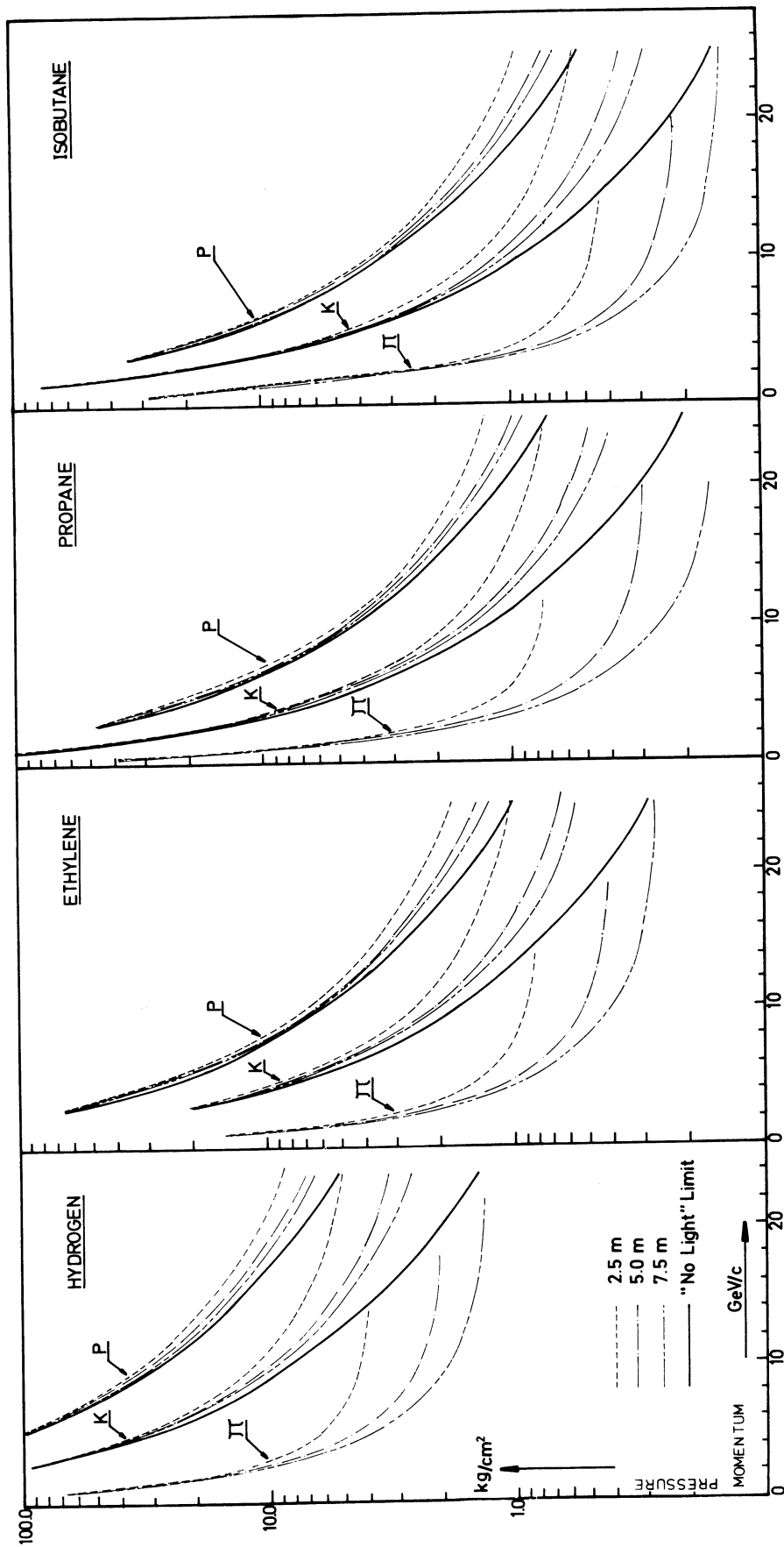
Fig.12



MEDIUM ANGLE SPECTROMETER

(HORIZONTAL PLANE)

Fig. 13



CERENKOV COUNTER THRESHOLD CURVES
FOR COUNTERS OF 2.5, 5.0 AND 7.5m LENGTH

Fig. 14

VACUUM CHAMBER FOR PARTICLE PRODUCTION EXPERIMENT

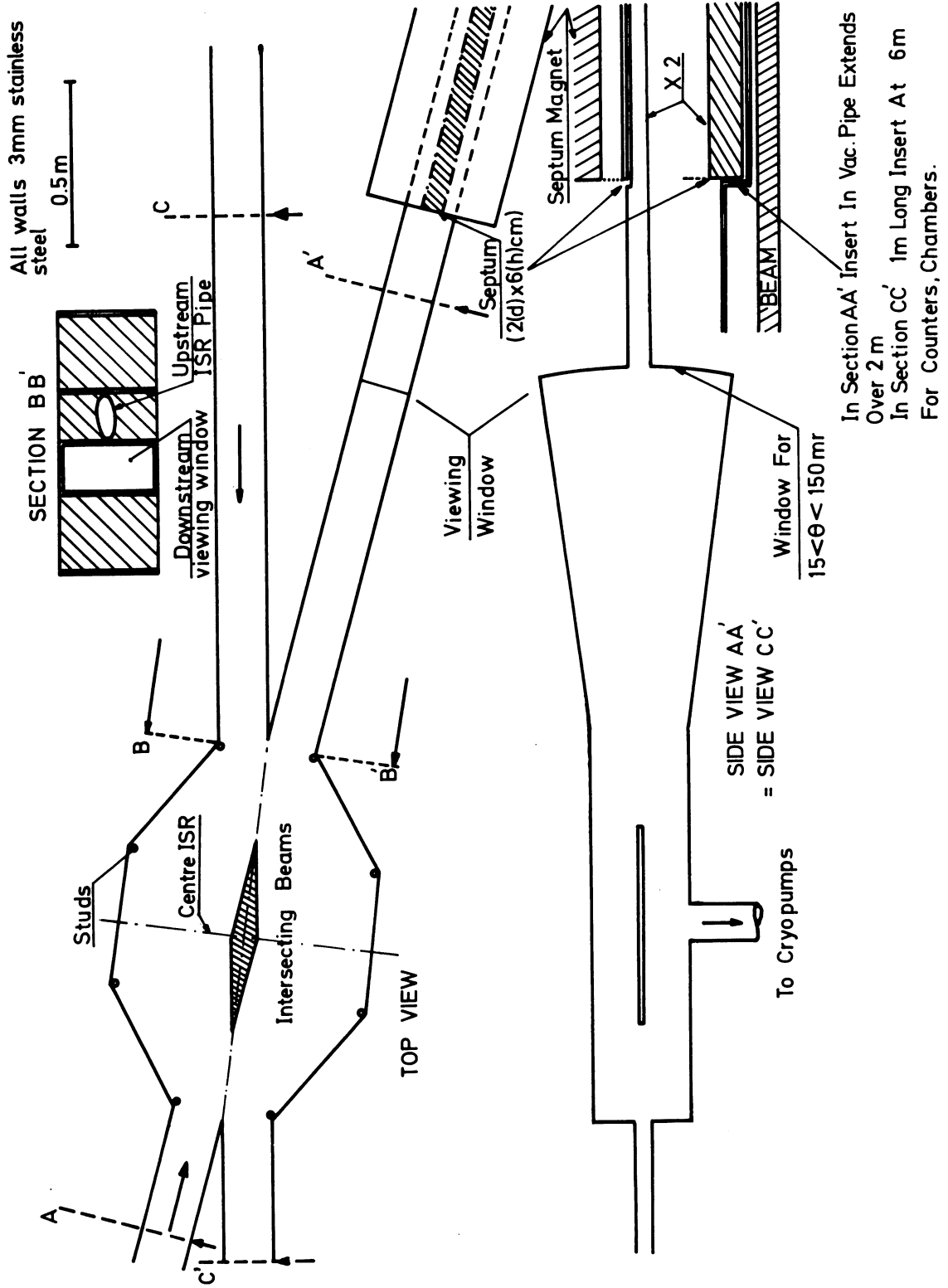


Fig. 15

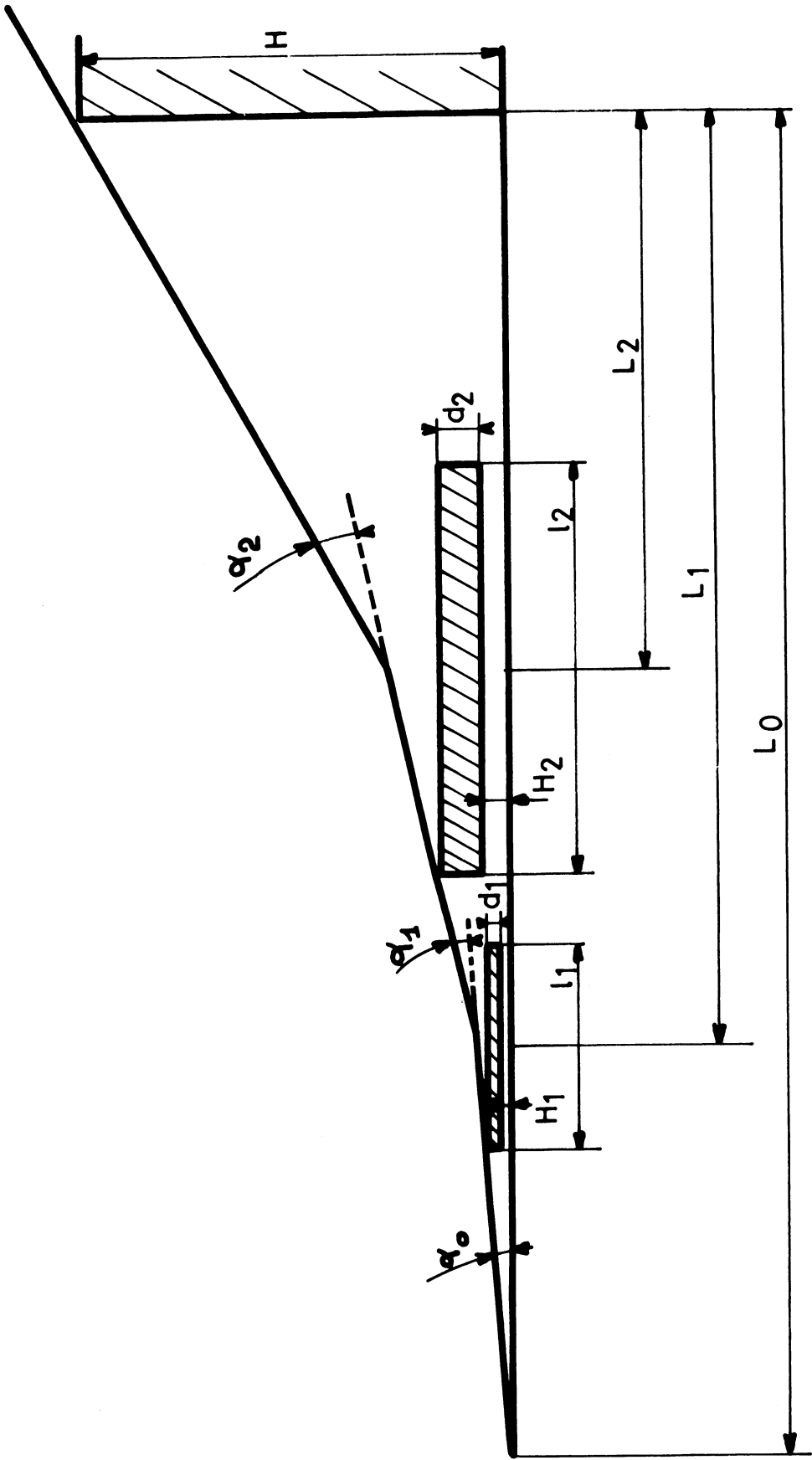
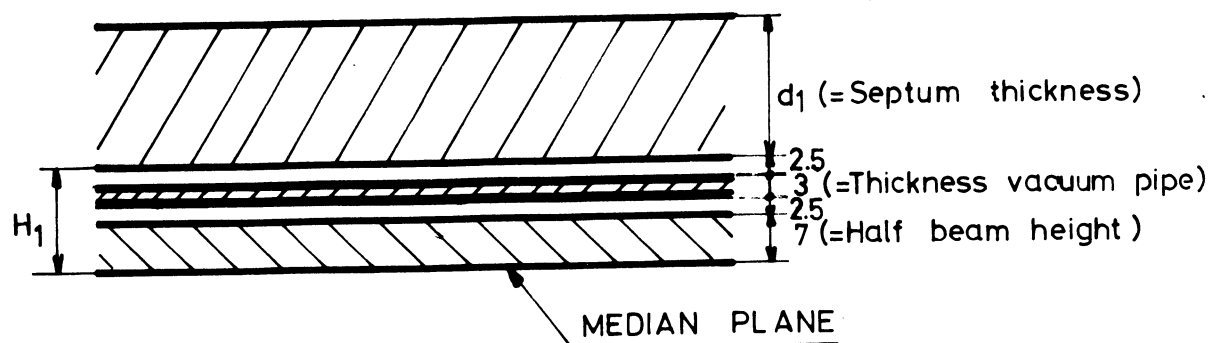
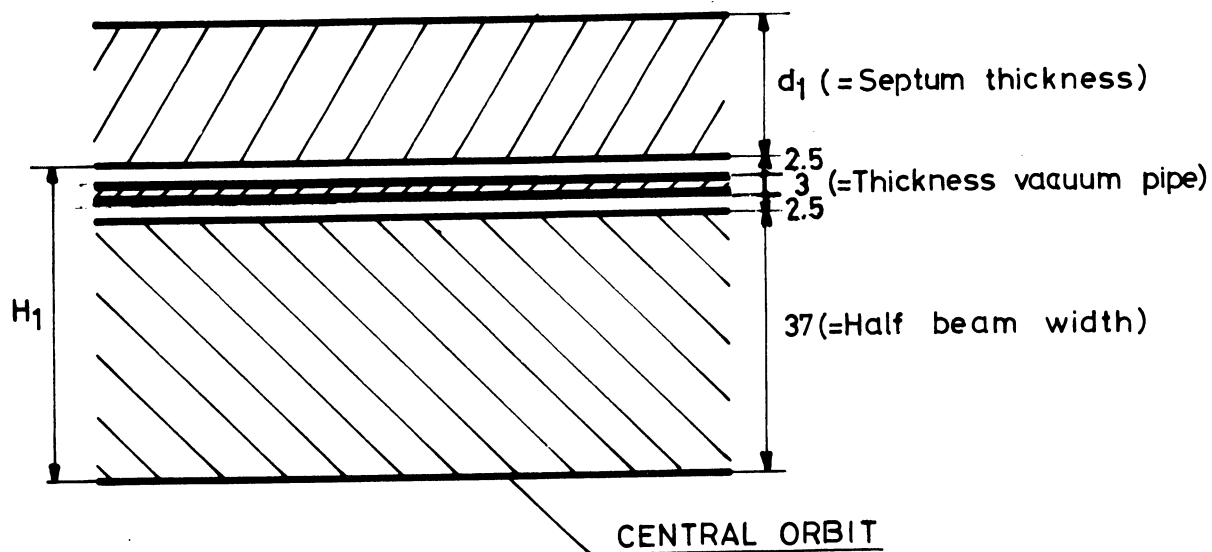


Fig. 16

VERTICAL BENDING



HORIZONTAL BENDING



All distances in mm

Fig. 17

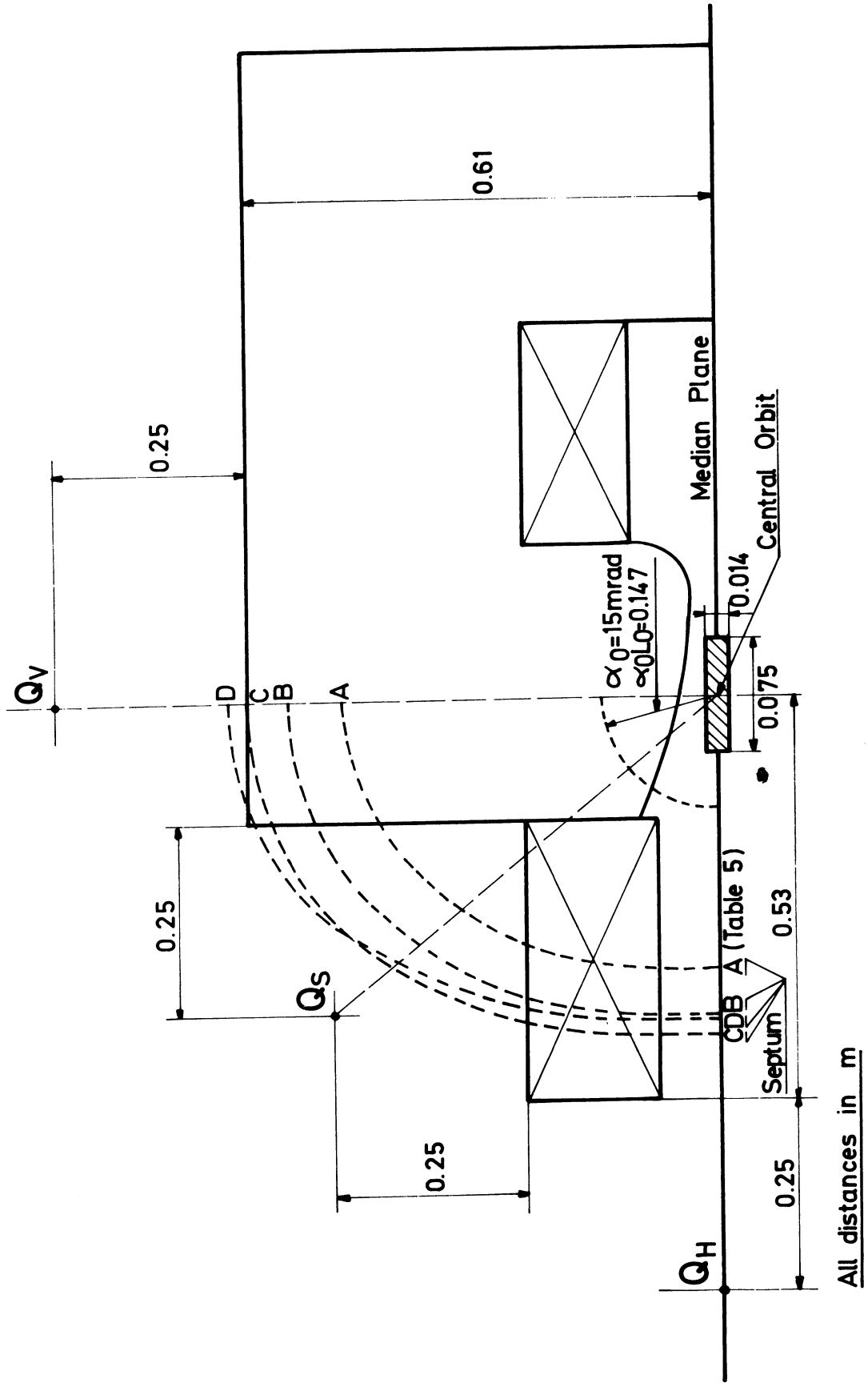


Fig. 18

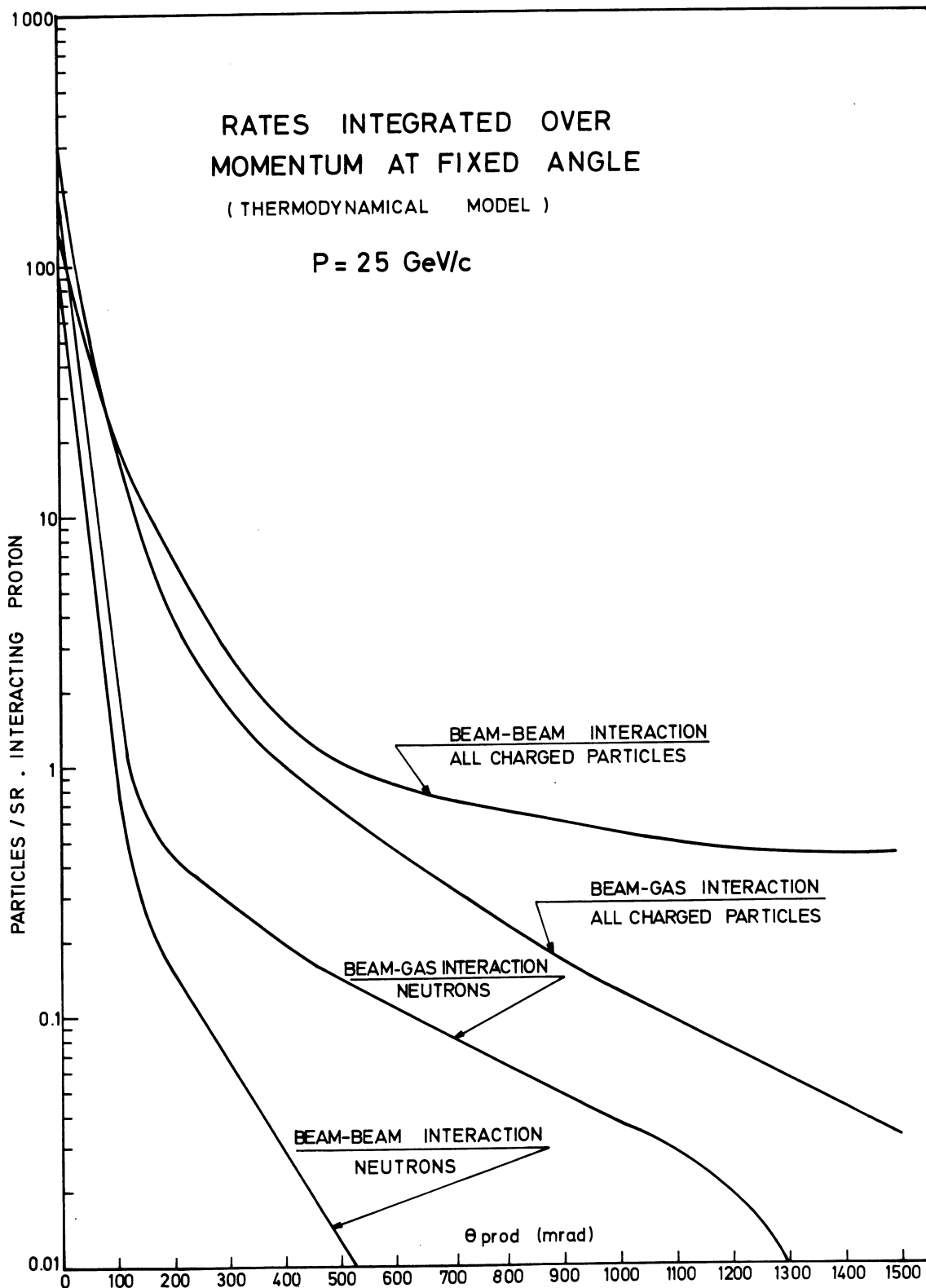


Fig. 19